

UNIVERSITY OF GRONINGEN

KAPTEYN INSTITUTE

BSC ASTRONOMY

Mid-IR Water Emission and the $10\text{ }\mu\text{m}$ Silicate Feature in Protoplanetary Disks Surrounding T Tauri Stars

Author:

JONAS BREMER

Supervisor:

PROF. DR. INGA KAMP

July 14, 2015

Abstract

To get an enhanced understanding of water in the planet forming region of protoplanetary disks, it is important to understand how dust, which is the main source of opacity affects the mid-IR emission of water. Therefore, this thesis presents a comprehensive study of the connection between the mid-IR water emission and the peak strength of the $10\text{ }\mu\text{m}$ silicate feature. Besides the investigation of observational data of TTauri disk systems that involved the analysis of Spitzer spectra, a detailed view on the influence of the structure of protoplanetary disks on these quantities is provided using the protoplanetary disk model (ProDiMo) from Woitke et al. (2009). Effects of grain growth, total disk gas mass and central star were explored. No correlation is found from the observations, but rather a diverse behavior between these quantities. Analysis of the silicate feature shows that sources with lower peak strengths of the silicate feature show larger degrees of crystallization. From the model series we find an anti-correlation between the mid-IR water emission and the peak strength of the $10\text{ }\mu\text{m}$ silicate feature, and showed that the peak strength of the $10\text{ }\mu\text{m}$ silicate feature is proportional to the bolometric luminosity. Our results show that dust significantly alters the emission of water, and thus reflects the fact that the amount of water emission that is observed from protoplanetary disks is not per se reflecting the abundance of water.

Contents

1	Introduction	2
2	Theory	3
2.1	Structure of protoplanetary disks	3
2.2	Structure and emission of the water molecule	4
2.3	Dust in protoplanetary disks	5
3	Analysis of observed data	7
3.1	Water emission	7
3.2	Silicate feature	7
3.3	Correlation	11
4	Modeling using ProDiMo	14
4.1	The standard model	14
4.2	Variation of dust properties	15
4.2.1	Variation of maximum grain size	15
4.2.2	Variation of the power-law index of the dust size distribution	22
4.3	Variation of the disks gas mass	28
4.4	Variation of the central star	30
4.5	Comparing modeled series	33
5	Comparison of observations with the models	34
6	Conclusion	36
7	Acknowledgments	37
8	Literature	38
	Appendices	40

1 Introduction

Ever since the beginning of modern civilization, mankind is wondering how the solar system was formed. Back in 1755 I. Kant developed an idea in which the solar nebula collapsed, resulting in a rotating disk in which a star and planets would form. These disks are now known as protoplanetary disks. Recent developments in technology and the ability to use telescopes in space opened the window for astronomers to study other solar systems in detail. Observations with the Hubble Space Telescope presented direct proof of protoplanetary disks (McCaughrean and O'Dell, 1996) through scattering and absorption of starlight. As we understand it now, protoplanetary disks are the result of star formation, which occurs through the collapse of dense molecular clouds of dust and gas. Conservation of angular momentum is what prevents gas and dust to collapse onto the central star. Consequently, a rotating disk like structure is formed as a result of the fact that gas and dust fall from the top and bottom of the cloud, meeting at the equatorial plane.

The main driver of the physical conditions such as temperature is the dust present throughout protoplanetary disks. Dust accounts for the bulk of the opacity and is responsible for the shielding of the intense UV and X-ray emission emanating from the central star. Re-radiation of the dust grains create an IR continuum within the disk which is an important mechanism for the excitation of molecules. The bulk of dust in protoplanetary disks is comprised of amorphous and crystalline silicates. These dust grains grow in size through processes such as coagulation (W.Barnes et al.) and dust settling. These processes eventually lead to the formation of planets. Throughout the process of planet formation, the gas content in the disks lowers through dissipation, since the amount of dust grains that shield the gas decreases. Eventually a debris disk is left with planets and planetesimals.

A variety of molecules are found in protoplanetary disks, including CO, CO₂, H₂O, HCN, OH and C₂H₂. Mid-infrared observations with the Spitzer Space Telescope indicate that the presence of water in protoplanetary disks surrounding low mass stars is not rare (Pontoppidan et al., 2010). Water is most frequently observed in protoplanetary disks surrounding T Tauri stars. T Tauri stars are active variable low mass ($< 2M_{\odot}$) pre-main-sequence stars of spectral type F-M, with strong X-ray and FUV emission (Henning and Semenov, 2013). Water is seen to be distributed throughout these disks; it is present in the gas phase in the inner warm regions ($<$ a few AU), whereas in the outer regions it is frozen out on dust grains. The region where this transition occurs is called the snow line. This molecule is an important component in planet formation; it is thought that water is incorporated in planets throughout the planet formation process (van Dishoeck, 2014). An increased understanding of water in the early phases of protoplanetary disks would give a better insight in the process of water delivery to planets, resulting eventually into oceans.

Future studies of the properties of water in protoplanetary disks require a better understanding of the interplay between molecular line emission and the properties of the dust e.g. how spectra emanate from T Tauri disk systems.

A brief description about the structure of protoplanetary disks, the structure of the water molecule and dust in protoplanetary disks will be given in Chapter 2. Chapter 3 of this thesis will cover the analysis of observational data followed by chapter 4 in which we use the ProDiMo model to simulate the effects of various parameters on the mid-IR water emission and the 10 μ m silicate feature. In Chapter 5, the results from the observations are compared to the model.

2 Theory

2.1 Structure of protoplanetary disks

Young stellar objects are classified by means of their spectral energy distribution (SED) which depends on their evolutionary phase. This classification scheme is known as the Lada sequence (Lada, 1987) and consists of 4 classes of objects, namely class 0, class I, class II and class III. Class 0 objects are cold pre-stellar dense cores embedded in an optically thick envelope of dust and gas. The SED is dominated by the far-IR regime. In class I objects, star-disk structures are present with the central star enhancing the temperature in the inner regions resulting in near-IR emission. These objects are still embedded in an envelope and so the SED peaks in the far-IR but shows a significant amount of radiation emitted in the near-IR. Once the star becomes hot enough and the envelope is removed by the radiation pressure, collapse of gas and dust onto the disk and accretion of material onto the central star, the central star becomes visible and only a disk is left. In addition to the optical, the excess of the SED of these objects covers the near to far-IR. These objects are classified as class II objects. In class 0, I, II objects, the central star accretes material from the disk. In class III objects the disk is cleaned to a large extent from gas and dust grains leaving planets and planetesimals (debris disk). The SED of these objects is to a large extent represented by the central star, therefore the amount of integrated IR radiation is very small e.g. $L_{\text{IR}}/L_* < 10^{-4}$. This thesis will cover T Tauri stars which belong to the class II objects (Mulders, 2013).

Observations with the Infrared Astronomy Satellite showed larger amounts of far-IR emission than predicted (Adams et al., 1987). In the same year Kenyon and Hartmann (1987) came to the conclusion that these objects possess flared disk structures based on the argument that more starlight is intercepted by the outer regions causing a stronger far-IR excess.

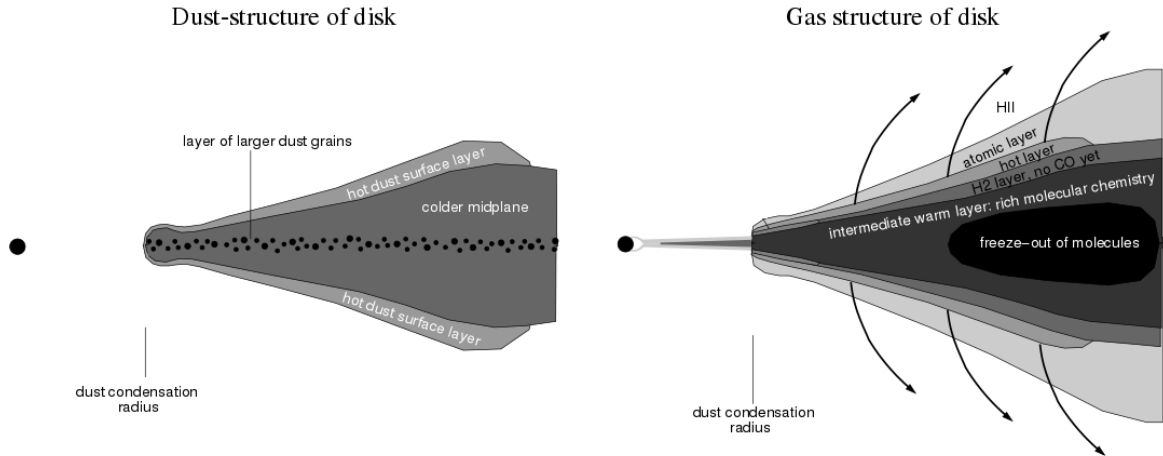


Figure 1: Schematic representation of the general gas and dust structure of a protoplanetary disk (Dullemond et al., 2007).

Protoplanetary disks come in a variety of sizes ranging from 10 to 1000 AU (Henning and Semenov, 2013). Due to the complex structure of these objects, they possess large variations in physical conditions with temperatures ranging from 10 K in the mid plane regions to 10000 K in the disk surface of the innermost regions. Densities of $< 10^4 \text{ cm}^{-3}$ up to 10^{15} cm^{-3} are present (Pontoppidan et al., 2014). Densities of protoplanetary disks are represented by the surface density, the surface density is defined as the vertical integrated density. In general, the surface density is described by a power law $\Sigma \propto r^{-p}$ with p usually in the 0-1 range (Williams and Cieza, 2011). The general structure of gas and dust in protoplanetary disks is shown in Fig. 1. One can distinguish between the vertical and radial structure of a protoplanetary disk. The vertical structure is divided into the surface layer, the intermediate region and the midplane (Pontoppidan et al., 2014). The surface layer is the optically thin region exposed to the UV photons and X-rays originating from the central star. The uppermost layers contain only atomic gas, since molecules are destroyed by the intense radiation field. Generally, temperatures in the surfaces layers are higher than in the inner regions. Gas temperatures encountered in surface layers

are higher than dust temperatures. As one gradually probes deeper regions, different molecules start to appear since different molecules require different energies to be destroyed and various chemical pathways to be formed. Molecules are destroyed by several processes including photo-dissociation ($XY + h\nu \rightarrow X + Y$) and dissociative recombination ($XY^+ + e^- \rightarrow X + Y$). One first encounters simple diatomic molecules as their formation only require one collision, whereas more complex molecules such as water require subsequent collisions and thus occur more frequently in denser regions. The intermediate layer, also known as the warm molecular layer is the region which is sufficiently shielded by small dust grains such that molecular gas can exist, providing a rich chemistry. This region is to a great extent dominated by the dust continuum. As one goes deeper in the disk the midplane region is encountered. This region is completely shielded from the intense radiation from the star resulting in temperatures that are sufficiently low such that molecules such as H_2O and HCN freeze out on dust grains (Walsh et al., 2013).

Radially disks are divided in the inner rim, the inner disk or planet forming region and the outer disk. The inner rim is the boundary of the dust free inner region that is typically located at ~ 0.02 AU for a T Tauri star (Dullemond and Monnier, 2010). This region has been cleared by the central star through sublimation of dust. Most of the near-IR emission originates from the inner dust rim which surrounds this region in which dust is heated to high temperatures. Further out, the planet forming region is encountered. This is the region in which molecules exist in the gas phase and it is characterized by the mid-IR dust continuum and mid-IR molecular emission. Besides the active chemistry in this region, dust processing is also active because of the relatively high orbital velocity compared to regions further out in the disk. Hence, in this region dust grains collide faster than regions that are at larger radii. The outer regions occupy the largest extent of protoplanetary disks, and are characterized by their large vertical extension. Therefore, large amounts of ice are present in the outer mid-planes.

2.2 Structure and emission of the water molecule

In order to interpret the emission of water, it is important to understand the structure and emission mechanisms of the water molecule. Water, or H_2O , is an asymmetric molecule that consists of two hydrogen atoms covalently bonded to one oxygen atom making it a polar molecule. The most abundant water isotope is $H_2^{16}O$. Since hydrogen atoms have a nuclear spin of $\frac{1}{2}$, the two hydrogen atoms can combine to form a singlet state ($S=0$) or a triplet state ($S=1$). Thus water exist in two forms, p- H_2O (para) which is the singlet state and o- H_2O (ortho) which is the triplet state (Poelman, 2007). Due to its asymmetric nature, it possesses a variety of degrees of freedom. These various degrees of freedom consist of quantized rotational and vibrational modes (Fig. 2). The vibrational modes are symmetric stretch, bending, anti-symmetric stretch whereas the rotational modes are defined as the rotation perpendicular to the inter-molecular axes (axes through the center of mass) A, B and C (Tennyson and Polyansky, 1998). The combination of vibrational and rotational energy states within an electronic energy state result in a large number of accessible quantum states each having a different energy. The general structure of the energy levels is shown in Fig. 2. An extremely large amount of transitions obeying the selection rules between these quantum states are possible, where most transitions consist of ro-vibrational ones. The transitions that are possible are governed by the selection rules, $J = 0 \pm 1$ and K_a, K_c can change by $\pm 1, \pm 3$ (Dionatos, 2015, in preparation). Emission lines are the result of excitation followed by de-excitation. Water molecules in protoplanetary disks are excited through several mechanisms such as collisions with other molecules, pumping through dust continuum radiation, photodesorption from dust grains (Meijerink et al., 2009). Rotational transitions occur predominantly in the mid and far infrared regime. The same notation for the rotational levels as in Pontoppidan et al. (2010) is adopted in which rotational levels are defined by $\mathbf{J}_{K_a K_c}$. J represents the main rotational quantum numbers with K_a and K_c being its projections on the inter-molecular axes A and C respectively. Since the rotational energy levels lie very close to each other, separate emission lines are hard to detect in spectra unless very high spectral resolution is used. Often blends are measured that consist of several emission lines. The blends that are studied in this thesis are the 15.17, 17.22 and the 29.85 μm blend. The wavelength range of these blends is determined through the modeled spectra in chapter 4. Water emission lines that make up these blends are listed in Table. 1.

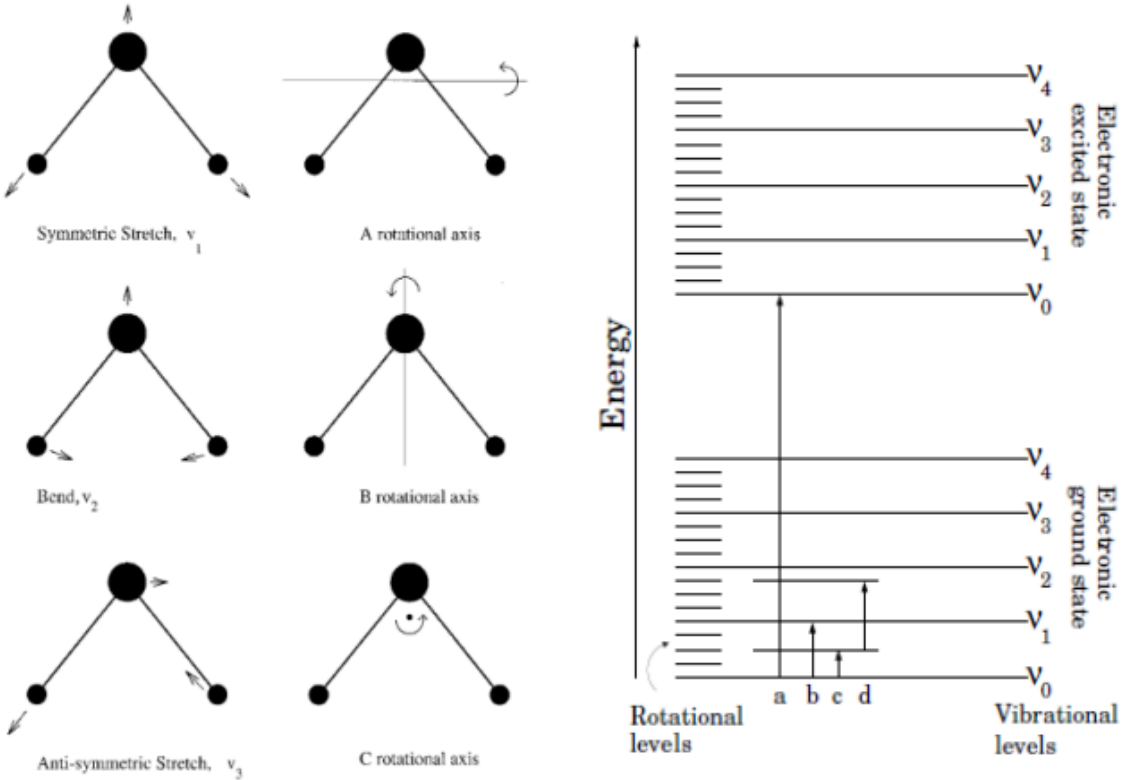


Figure 2: left: visualization of the various vibrational and rotational modes of the water molecule (Tennyson and Polyansky, 1998); right: structure of the energy levels of the water molecule (Poelman, 2007).

2.3 Dust in protoplanetary disks

Physical conditions such as density and temperature within protoplanetary disks are to a great extent determined by dust. Dust regulates the transmission of intense radiation from the central star through scattering and absorption. Although dust only represents a small fraction of the mass of protoplanetary disks, it is the dominant source of opacity. The bulk of the opacity is invoked by the smallest grains. Distributions of dust grains sizes are usually represented by means of a power law, $n(a) \sim a^{-a_{\text{pow}}}$ (Antonellini et al., 2015b, under revision). This power law indicates how many grains of a certain size represent the overall population of dust grains. Consequently the smallest grains represent the largest population of dust grains. Small grains dominate the surface area whereas large grains dominate the mass. As a result of processes such as dust settling and coagulation, the size of dust grains increases when propagating towards the midplane, representing the first steps towards planet formation. Coagulation is the process in which dust grains combine through collisions to form larger grains. Dust settling refers to the process in which dust grains migrate towards the mid-plane as a consequence of gravity. In addition to grain growth, dust in protoplanetary disks evolves in composition. An example is the crystallization of amorphous dust grains that takes place through processes such as thermal annealing in the inner regions of protoplanetary disks. The majority of dust in protoplanetary disks consists of silicates. The ones that are observed most frequently are amorphous olivines, pyroxenes and the crystalline silicates, enstatite (MgSiO_3) and forsterite (Mg_2SiO_4) (Kessler-Silacci et al., 2007). The fact that no crystalline silicates are found in the ISM (K.Demyk et al. 2000) as opposed to protoplanetary disks tells us that various processes change the structure and composition of the dust. The composition of dust thus gives indications of the evolutionary state of dust in protoplanetary disks. Silicates are observed to have two prominent emission features in the mid-IR. The $10 \mu\text{m}$ feature which is produced through stretching of Si-O bonds and the $20 \mu\text{m}$ feature that is produced via Si-O-Si bending. Of these two, the $10 \mu\text{m}$ emission feature is the dominant one. Most of the $10 \mu\text{m}$ dust emission has its origin in the inner disk regions close to the star. This is because of the fact that dust temperatures in these regions are sufficiently high to satisfy the conditions that are needed to produce the $10 \mu\text{m}$ silicate feature. Since

Table 1: Transitions for the lines that are present in the blends

Blend	J	K _a	K _c	⇒	J	K _a	K _c	ortho/para	λ [μm]	A _{ul} [s ⁻¹]
15.17 μm										
	10	6	5		9	3	6	ortho	15.15072	6.517·10 ⁻¹
	8	7	2		7	4	3	ortho	15.16408	6.551·10 ⁻²
	5	4	1		4	3	2	ortho	15.18890	1.084·10 ⁻¹
	10	6	4		9	3	7	para	15.16920	4.208·10 ⁻¹
	15	10	6		15	7	9	para	15.17165	1.037·10 ⁻¹
	5	4	2		4	3	1	para	15.17313	2.241·10 ⁻¹
17.22 μm										
	13	4	9		12	3	10	ortho	17.19351	6.095
	15	9	6		14	8	7	ortho	17.22848	5.209·10 ¹
	9	6	4		8	3	5	para	17.20910	3.389·10 ⁻¹
	12	3	9		11	2	10	para	17.21965	2.557
	11	3	9		10	0	10	para	17.22545	9.619·10 ⁻¹
	15	9	7		14	8	6	para	17.23497	5.205·10 ⁻¹
29.85 μm										
	6	5	2		6	2	5	ortho	29.78962	1.319·10 ⁻²
	7	2	5		6	1	6	ortho	29.83672	5.072·10 ⁻¹
	8	5	4		9	0	9	ortho	29.85089	1.641·10 ⁻⁴
	18	1	18		17	0	17	ortho	29.86540	1.623·10 ¹
	15	3	12		14	4	11	ortho	29.92620	9.683
	8	3	5		7	2	6	para	29.75330	1.649
	13	4	10		12	3	9	para	29.80668	7.446
	18	0	18		17	1	17	para	29.86546	1.623·10 ¹
	5	4	2		4	1	3	para	29.88488	8.560·10 ⁻²

The left column of quantum states represent the upper state, the right represents the lower state. These energy states for the water molecule are obtained from Tennyson et al. (2001). The width of these blends is obtained from the modeled mid-IR spectrum the will be described in Chapter 4. A_{ul} denotes the probability per unit time for spontaneous emission from the upper to the lower state. Note that the 29.85089 μm line does not obey the selection rules.

protoplanetary disks have high dust opacities at IR wavelengths, silicate features in the mid-IR range originate from the upper layers and only give information about dust grains in the $\tau \sim 1$ layers (Natta et al., 2007). Mainly grains with temperatures in the range of 200K-600K are measured by the 10 μm spectral region (Natta et al., 2007). In addition to the temperature range, the 10 μm feature only traces grains that are smaller than a few microns (Natta et al., 2007). It was shown that the strength of the 10 μm is inversely correlated to the dust grain size (van Boekel et al., 2003). In addition to the grain size, it was also shown that the silicate feature depends on the composition of the dust (Kessler-Silacci et al., 2005). The silicate feature thus constitutes an important tool for studying the properties of the dust in protoplanetary disks.

3 Analysis of observed data

In this Chapter, mid-IR water emission and the $10\ \mu\text{m}$ silicate feature of observed TTauri disk systems will be studied to find out whether there is a correlation between the mid-IR water emission and the silicate feature and how they correlate.

3.1 Water emission

A detailed analysis of mid-IR molecular emission from protoplanetary disks was made by Pontoppidan et al. (2010). In their work, a large collection of T Tauri disks were studied by detailed analysis of spectra in the mid-IR range that were observed with the Infrared Spectrograph on the Spitzer Space Telescope. The spectra they used were obtained with the infrared spectrograph modules SH (Short High) and LH (Long High) covering a combined range of $9.9 - 37.2\ \mu\text{m}$ with a resolution of 600. Most of the spectra they used were observed in the T Tauri c2d program (Evans et al., 2003) and program 50641 (John Carr). They detected water in numerous disks at the $3.5\ \sigma$ level. Integrated blend fluxes for these sources were determined from line blends at $15.17, 17.22$ and $29.85\ \mu\text{m}$ by fitting a Gaussian positioned on a linear continuum. Values of integrated blend fluxes from their work will be used for further analysis. They selected these blends since they are most isolated from other emission lines. Sources in which Pontoppidan et al. (2010) detected water are investigated further in this study.

3.2 Silicate feature

In this analysis we will focus on the peak strength of the silicate feature since this is a property of the silicate feature that is sensitive to the size and composition of dust grains. Throughout this thesis we calculate the peak strength of the silicate feature as

$$S_{\lambda,\text{peak}} = \frac{F_{\lambda} - F_{\lambda,\text{cont}}}{F_{\lambda,\text{cont}}} \quad (1)$$

where F_{λ} represents the flux of the spectrum at λ and $F_{\lambda,\text{cont}}$ is the flux of the fitted local continuum at λ . The numerator represents the peak flux of the silicate feature. Since we do not want to have a selection bias based on the intrinsic brightness of the sources in the results, the peak flux of the silicate feature is divided by the local continuum at λ . Therefore, the peak strength of the silicate feature represents the relative measure of the peakflux of the silicate feature with respect to the local continuum. The peak strength of the silicate feature will be determined at $\lambda = 10\ \mu\text{m}$. Because of the lack of information in the literature about the peak strength of the $10\ \mu\text{m}$ silicate feature for these TTauri objects in which water was detected, archived Spitzer spectra will be analyzed.

To study the silicate feature, Spitzer spectra are needed that were observed with the SL (Short Low) modules; they cover the wavelength range of the silicate feature and have a low resolution of 60-120. Since we are only interested in the peak strength of the silicate feature, no high resolution spectra are required for this analysis of the silicate feature. The SL spectrum was only available for part of the selected objects in which water was detected by Pontoppidan et al. (2010), thus reducing the extent of the sample. Part of the spectra were obtained through private contact with F.Lahuis; these spectra were observed as part of the c2d program (Evans et al., 2003). Data reduction of these spectra is described in Lahuis (2007). Additional spectra are retrieved from the CASSIS database¹ (Lebouteiller et al., 2011). For these spectra, an explanation of the data reduction procedure is given in Lebouteiller et al. (2011). Sources that were selected for this study are listed in Table 2. This sample of TTauri stars consists of a variety of spectral classes ranging form M1 to G5, although the majority consists of early K and late M classes.

The spectra with their silicate features are shown in Fig. 3. A range of variation in the properties of the silicate features in this sample of disks is noticed. Shapes vary from flat features to significantly peaked structures. Variations in strength of the silicate features indicate that dust processing is active

¹The Cornell Atlas of Spitzer/IRS Sources (CASSIS) is a product of the Infrared Science Center at Cornell University, supported by NASA and JPL.

and that properties such as grain sizes and composition of dust vary throughout this sample. It is known that the silicate feature decreases in strength and widens with increasing sizes of dust grains (Voshchinnikov et al., 2008). Some silicate features are centered at longer wavelengths and contain substructures; this is an indication that crystallization of amorphous silicates takes place (Kessler-Silacci et al., 2005). However, varying disk geometries can also contribute to the difference in the silicate features. It has been found that the silicate feature becomes stronger with increasing degree of flaring. (Bouwman et al., 2008). Difference in the degree of crystallization together with the fact that the process of crystallization seems to be independent of the spectral type (Olofsson et al., 2010), tells us that dust in these disks is in different evolutionary stages.

To determine the peak strength of the silicate feature, the net flux contribution of the silicate feature needs to be calculated. The first step is a continuum fit that covers the whole feature. This is achieved by selecting two data points in the region on both sides of the silicate feature where the feature starts to appear. Manual selection of these points is required since the silicate features are different from spectrum to spectrum. The wavelength range that is used for the selection of points to the left of the feature is 7.70-7.88 μm , whereas the wavelength range of the right of the feature is selected to be 12.54-13.93 μm . The continuum is fit by a linear function; this function will be determined at each wavelength of the spectrum that covers the silicate feature. This fit is made using the `scipy.optimize.curve_fit` python module which applies the method of non-linear least squares. The optimal parameters are evaluated by this module through minimization of the sum of the residuals, in which the uncertainties in the data are included as weights

$$\chi^2 = \sum_i \left(\frac{a\lambda[i] + b - \text{flux}_{\text{data}}[i]}{\sigma_{\text{data}}} \right)^2. \quad (2)$$

From the uncertainties in the parameters in the fit that are evaluated by this module, two lines y_1 and y_2 with the largest deviations from the fit are evaluated

$$y_1 = (a_{\text{opt}} + \sigma_a)\lambda + (b_{\text{opt}} - \sigma_b) \quad (3)$$

$$y_2 = (a_{\text{opt}} - \sigma_a)\lambda + (b_{\text{opt}} + \sigma_b) \quad (4)$$

where a_{opt} and b_{opt} are the parameters of the best fit with their corresponding uncertainties σ_a and σ_b . The maximum difference between the fit and one of these lines at the wavelength at which the peak strength will be determined, is used as the uncertainty in the continuum

$$\sigma_{\text{cont}} = \max(|y_{\text{fit}} - y_1|; |y_{\text{fit}} - y_2|). \quad (5)$$

The continuum is subtracted from the spectrum resulting in the net flux contribution of the silicate emission feature. The following relation is used for the propagation of uncertainties in the subtraction of the continuum

$$\sigma_{\lambda, \text{peak}} = \sqrt{\sigma_{\lambda, \text{flux}}^2 + \sigma_{\lambda, \text{cont}}^2} \quad (6)$$

where $\sigma_{\lambda, \text{peak}}$ is the uncertainty in the peak flux at λ , $\sigma_{\lambda, \text{flux}}$ is the uncertainty in the flux of the spectrum at λ and $\sigma_{\lambda, \text{cont}}$ indicates the uncertainty in the fitted continuum at λ . Dividing the peak flux of the silicate feature by the fitted continuum at the desired wavelength requires further propagation of uncertainty giving us the uncertainty in the peak strength of the silicate feature

$$\sigma_{S_{\lambda, \text{peak}}} = \sqrt{\left(\frac{1}{F_{\lambda, \text{cont}}} \right)^2 \sigma_{\lambda, \text{peak}}^2 + \left(\frac{F_{\lambda, \text{peak}}}{F_{\lambda, \text{cont}}^2} \right)^2 \sigma_{\lambda, \text{cont}}^2}. \quad (7)$$

Continuum subtracted silicate features together with the continuum fit are shown in Fig. 3. Peak fluxes are determined from these continuum subtracted silicate features. To prevent increases in uncertainties by further interpolations, the flux at the measured wavelength closest to 10 μm is determined. These wavelengths lie in the range of 9.96-10 μm , and the flux changes only by small amounts over this wavelength range.

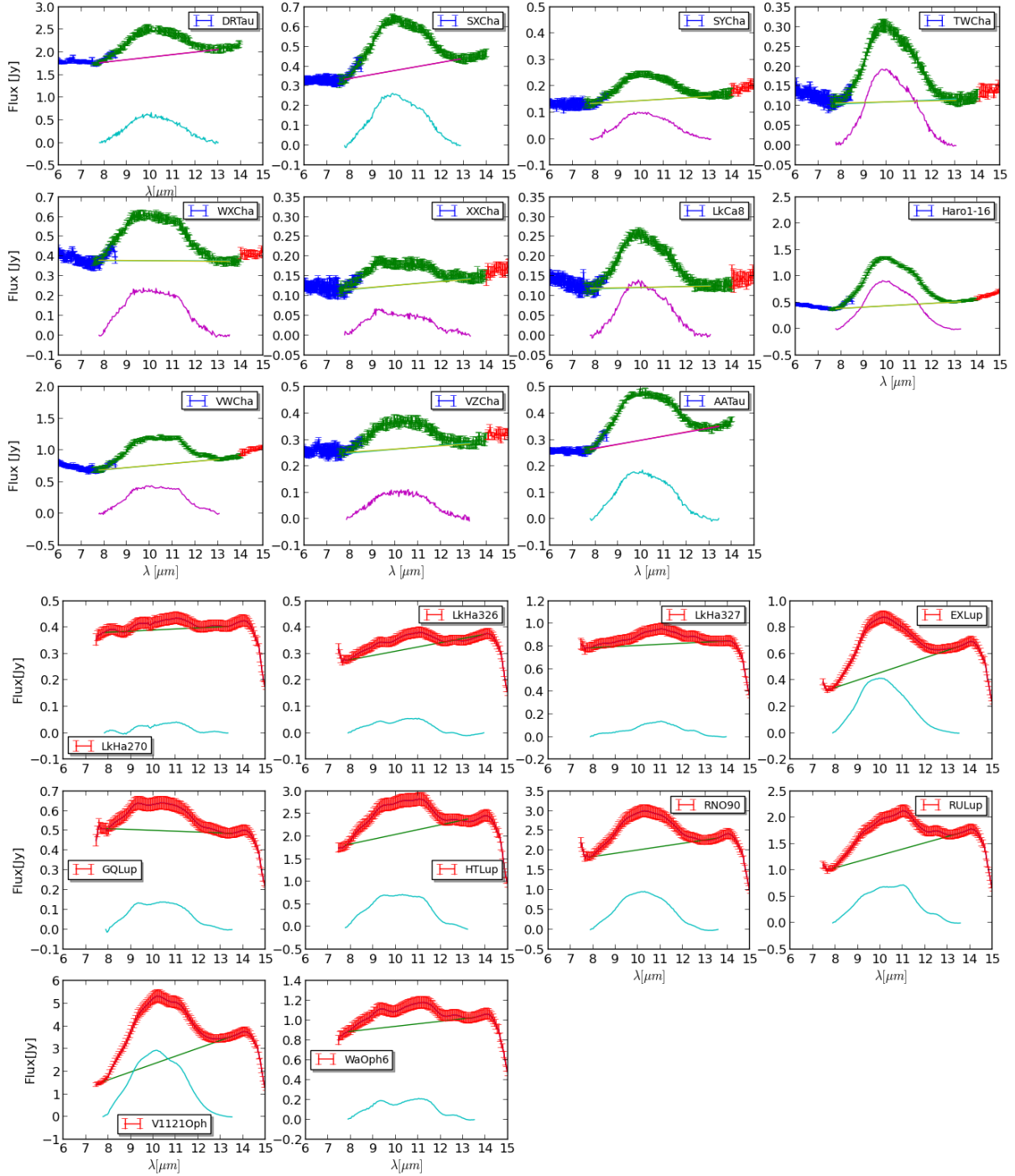


Figure 3: Spitzer spectra in the mid-IR range for the selected targets. Together with the silicate feature, the continuum fit and the continuum subtracted silicate features are shown. The three rows on the top show the spectra the are obtained from the CASSIS database; blue indicates the SL2 module that covers the $5.2\text{--}8.7\,\mu\text{m}$ range, green indicates the SL1 module which covers a region of $7.4\text{--}14.5\,\mu\text{m}$ and red represents the LL2 module with a range of $14.0\text{--}21.3\,\mu\text{m}$. The three bottom rows show the spectra obtained by private contact with F. Lahuis, these spectra cover the $7.4\text{--}14.5\,\mu\text{m}$ range of the SL1 module. The straight line in all the plots represents the continuum fit. Continuum subtracted silicate feature are shown in purple and light blue, this difference in color is a result from the plotting procedure and has no physical meaning.

Table 2: Selected T Tauri disk systems

Source Name	Spectral Type ¹	Distance ¹ [pc]	Luminosity ² [L_{\odot}]	15.17 μm^1			17.22 μm^1			29.85 μm^1			Peak Strength of the 10 μm silicate feature			Accretion rate ² $\log(\text{M}_{\odot}\text{yr}^{-1})$		
				[$10^{-14} \text{erg cm}^{-2} \text{s}^{-1}$]	[$10^{-14} \text{erg cm}^{-2} \text{s}^{-1}$]	[$10^{-14} \text{erg cm}^{-2} \text{s}^{-1}$]	[$10^{-14} \text{erg cm}^{-2} \text{s}^{-1}$]											
LkHa 270	K7	250	...	< 0.36	0.47 ± 0.05	0.62 ± 0.05	< 0.34	0.62 ± 0.05	0.62 ± 0.05	0.82 ± 0.07	0.82 ± 0.07	0.20 ± 0.17		
LkHa 326	M0	250	...	1.00 ± 0.27	2.43 ± 0.25	2.31 ± 0.15	1.00	2.43 ± 0.25	2.31 ± 0.15	0.30 ± 0.04	0.30 ± 0.04	0.43 ± 0.18		
LkHa 327	K2	250	...	< 0.37	1.28 ± 0.12	4.05 ± 0.07	0.39	1.28 ± 0.12	4.05 ± 0.07	1.04 ± 0.11	1.04 ± 0.11	0.35 ± 0.17		
EXLup	M0	150	0.39	0.71 ± 0.06	0.71 ± 0.06	0.71 ± 0.06	0.80	0.71 ± 0.06	0.71 ± 0.06	1.33 ± 0.04	1.33 ± 0.04	0.30 ± 0.07	-8.00/-7.00		
GQ Lup	K7	150	1.45	< 1.75	2.50 ± 0.13	3.49 ± 0.14	1.45	< 1.75	2.50 ± 0.13	2.41 ± 0.08	1.17 ± 0.15	1.17 ± 0.15	0.39 ± 0.08	
HTLup	K2	150	0.42	1.12 ± 0.30	2.69 ± 0.32	2.54 ± 0.17	1.25	1.12 ± 0.30	2.69 ± 0.32	0.99 ± 0.09	0.99 ± 0.09	0.61 ± 0.09	-7.70	-7.05	-7.05	-7.05		
RULup	K7	150	...	5.83 ± 0.24	10.10 ± 0.25	5.86 ± 0.14	125	5.83 ± 0.24	10.10 ± 0.25	5.86 ± 0.14	5.86 ± 0.14	0.37 ± 0.06		
V1121Oph	K4	125	...	0.83 ± 0.07	1.56 ± 0.08	1.44 ± 0.06	125	0.83 ± 0.07	1.56 ± 0.08	1.54 ± 0.07	1.54 ± 0.07	1.44 ± 0.06		
RNO90	G5	125	...	1.57 ± 0.07	2.50 ± 0.19	3.73 ± 0.10	125	1.57 ± 0.07	2.50 ± 0.19	7.13 ± 0.19	7.13 ± 0.19	3.73 ± 0.10	0.13 ± 0.05	-6.64	-6.64	-6.64		
Haro 1-16	K2-3	200	0.67	4.53 ± 0.19	7.13 ± 0.19	3.73 ± 0.10	140	2.50	4.53 ± 0.19	7.13 ± 0.19	3.73 ± 0.10	3.73 ± 0.10	0.33 ± 0.04	-6.50/-6.25	-6.50/-6.25	-6.50/-6.25		
WaOph6	K	125	...	0.48 ± 0.06	1.48 ± 0.06	0.74 ± 0.03	140	0.98	0.48 ± 0.06	1.48 ± 0.06	0.74 ± 0.03	0.74 ± 0.03	0.60 ± 0.02	-8.48/-8.19	-8.48/-8.19	-8.48/-8.19		
DR Tau	K7	140	...	< 0.17	0.27 ± 0.05	0.71 ± 0.06	140	...	0.27 ± 0.05	0.27 ± 0.05	0.71 ± 0.06	0.71 ± 0.06	1.63 ± 0.04		
AA Tau	K7	140	...	1.99 ± 0.07	3.54 ± 0.08	1.81 ± 0.04	140	2.34	1.99 ± 0.07	3.54 ± 0.08	1.39 ± 0.05	1.39 ± 0.05	0.13 ± 0.05	-6.64	-6.64	-6.64		
LkCa8	M0	140	...	0.94 ± 0.05	1.39 ± 0.05	0.75 ± 0.02	180	0.46	0.94 ± 0.05	1.39 ± 0.05	1.21 ± 0.06	1.01 ± 0.04	0.65 ± 0.07		
VW Cha	M0.5	180	...	0.78 ± 0.06	1.21 ± 0.06	1.01 ± 0.04	180	0.44	0.78 ± 0.06	1.21 ± 0.06	0.12 ± 0.03	0.43 ± 0.02	1.12 ± 0.10	-8.37	-8.37	-8.37		
VZ Cha	K6	180	...	< 0.09	1.04 ± 0.03	0.95 ± 0.04	180	0.37	< 0.09	1.04 ± 0.03	0.55 ± 0.02	0.55 ± 0.02	1.11 ± 0.14	-8.37	-8.37	-8.37		
SX Cha	M0	180	...	0.61 ± 0.02	1.61 ± 0.04	1.03 ± 0.06	180	0.90	0.61 ± 0.02	1.61 ± 0.04	0.90 ± 0.02	0.90 ± 0.02	2.90 ± 0.23		
SY Cha	M0	180	...	1.09 ± 0.04	1.61 ± 0.04	1.03 ± 0.06	180	0.68	1.09 ± 0.04	1.61 ± 0.04	1.03 ± 0.06	1.03 ± 0.06	1.03 ± 0.06	-8.47	-8.47	-8.47		
TW Cha	K7	180	...	0.40 ± 0.03	0.46 ± 0.03	0.40 ± 0.02	180	0.26	0.40 ± 0.03	0.46 ± 0.03	0.40 ± 0.02	0.40 ± 0.02	0.70 ± 0.11	9.07	9.07	9.07		

References: (1) Pontoppidan et al. (2010); (2) Salyyk et al. (2011).

3.3 Correlation

In order to interpret these results and see how they compare from disk to disk, the distance has to be taken into account (Table 2). Distances are normalized to 140 pc as this is also the distance used in the TTauri disk model (Chapter 4). A factor of

$$\frac{d[\text{pc}]}{140[\text{pc}]^2} \quad (8)$$

is used for this normalization. Integrated water line fluxes (Pontoppidan et al., 2010) together with the resulting peak strength of the $10\ \mu\text{m}$ silicate feature are plotted in Fig. 4 and are listed in Table 2.

Peak strengths of the silicate feature in this sample range from 0.13 to 2.90 whereas integrated water blend fluxes of $0.20 \cdot 10^{-14}\ \text{erg cm}^{-2}\ \text{s}^{-1}$ to $8.05 \cdot 10^{-14}\ \text{erg cm}^{-2}\ \text{s}^{-1}$ are found. From the result, we find no clear correlation between the mid-IR water blend fluxes and the peak strength of the $10\ \mu\text{m}$ silicate feature but rather a large scatter. This might be a possible indication for the various physical properties of these disks. Some aspects however are noticed in this sample. Two groups are distinguished, namely a group that shows large water blend fluxes compared to the majority and a group which shows less variation in water blend fluxes which represents the majority.

We find that the majority of the sources are found below a water blend flux of $2.5 \cdot 10^{-14}\ \text{erg s}^{-1}\ \text{cm}^{-2}$. Since these are disks from a variety of star forming regions, this could be a typical value for the mid-IR water emission emanating from TTauri stars.

It is interesting to note that some disks (case 1) show large variations in water blend fluxes in a small range of $10\ \mu\text{m}$ peak strengths whereas other disks (case 2) show large variations in the $10\ \mu\text{m}$ peak strength in a small range of water line fluxes. In order to understand this behavior and provide possible explanations for it, additional information for the sample of sources is obtained from the literature. Values for the bolometric luminosity, mass accretion rates (Table 2) (Salyk et al., 2011) and Far Ultra Violet (FUV) ($\lambda = 125\text{-}170\ \text{nm}$) luminosity (Yang et al., 2012) are collected, these values however were not available for all sources.

Considering the case 1 sources that show variation in water blend fluxes in a small range of peak strengths of the silicate feature, we note the following. Some sources show an increase in water blend fluxes with bolometric luminosity whereas other sources show increase in water blend fluxes at a similar or lower bolometric luminosity. We do not expect the properties of dust to vary significantly for a small range of peak strengths. Larger luminosities will enhance the radiation field leading to increased water line emission. This was shown by Antonellini et al. (2015a, under revision) who found a direct correlation between the luminosity and the mid-IR water emission through modeling of different central stars.

Several explanations could account for the other the behavior of case 1 sources in which we find different blend fluxes for similar luminosities or higher water blend fluxes for lower luminosities. A possible explanation lies in the FUV radiation field that is produced by accretion of material onto the central star. We find that some of the sources with larger water blend fluxes show larger accretion rates compared to the average. Larger accretion rates result in enhanced FUV fields contributing to increased heating of gas and thus enhancing line emission. Mid-IR water line emission was shown to be correlated with the FUV luminosity (Antonellini et al., 2015a, under revision). In addition, this idea is supported by the fact that we find no correlation between the peak strength of the silicate feature and the FUV luminosity as shown in Fig. 5. Another explanation for the fact that we find we different blend fluxes for similar luminosities or higher water blend fluxes for lower luminosities, could be an effective vertical transport of water in these disks to the upper layers enhancing the extent of the emission region resulting in higher water line fluxes.

When considering the case (2) sources that show large variation in the peak strength of the silicate feature in a small region of water blend fluxes, it seems that variation in dust opacities is not affecting the emission of water and rather suggests the independent nature between these quantities. On the other hand, it is noted that sources which show the highest blend fluxes have low peak strengths of the silicate feature. Whereas at the largest peak strengths, water blend fluxes seem to be lower than average.

This could indicate an inverse trend in which the amount of observed water blend fluxes decrease with increasing peak strengths of the silicate feature. Differences in blend fluxes between the 15.17, 17.22 and 29.85 μm blends are most likely the result of the fact that these lines trace different regions of the disk (Meijerink et al., 2009) having different radial extensions.

We find no clear evidence for a correlation between the bolometric luminosity and the peak strength of the 10 μm silicate feature, this is shown in Fig. 5. Variations in the peak strength of the silicate feature are noted in a small range of luminosities. The most likely explanation for these findings is that the dust in these disks is in a different evolutionary state in which the grains have grown to various extents reducing peak strength of the silicate feature. Another possible explanation for the absence of a correlation between the bolometric luminosity and the peak strength of the 10 μm silicate feature lies in the geometry of the disks. As mentioned previously, it is known that the silicate feature becomes stronger with increasing degree of flaring (Bouwman et al., 2008). As some spectra show clear signs of crystallized dust in these objects, quantification of the degree of crystallization will give a better insight in the evolutionary state of the dust. We will use a method similar to the one used by Olofsson et al. (2009) for this quantification. The ratio of the flux at 11.3 μm with respect to the flux at 9.8 μm of the continuum subtracted silicate feature is used for the measure of crystallization. Large ratios indicate increased degrees of crystallization. A ratio of 0.75 is adopted above which the sources were selected to contain sufficient degree of crystallization. These sources are shown in red in Fig. 4. It becomes clear that the majority of sources which contain low peak strengths show signs of crystallized dust. This is consistent with the finding of van Boekel et al. (2005) who show that disks with lower peak strength show larger degrees of crystallization.

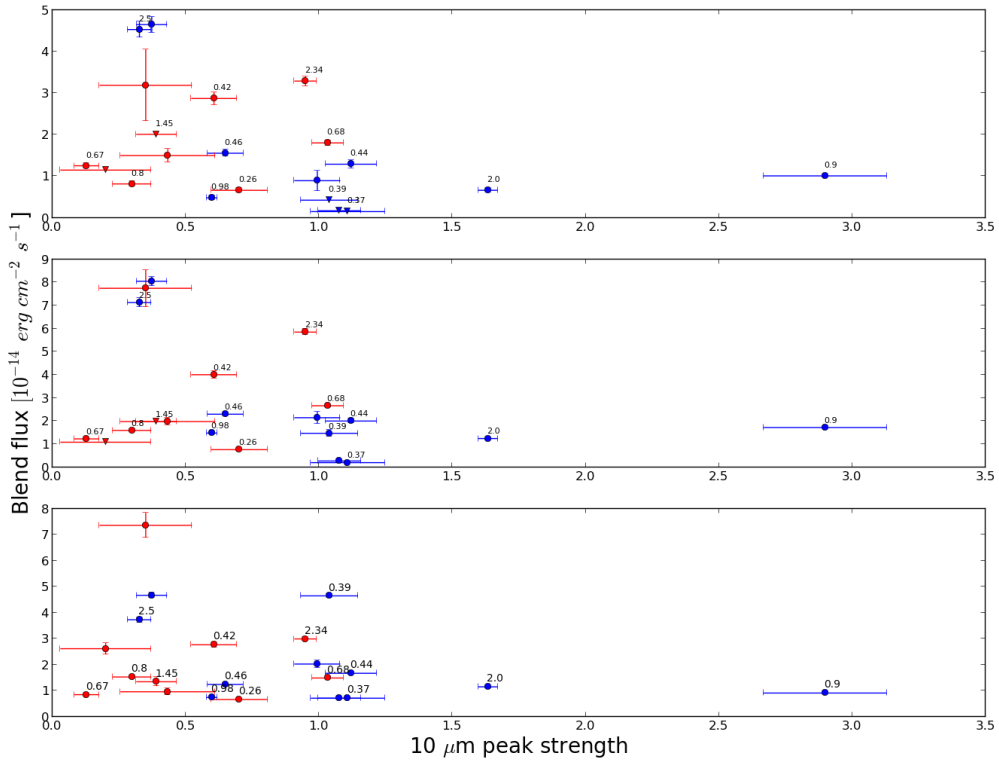


Figure 4: Mid-IR integrated water blend fluxes versus the peak strength of the 10 μm silicate feature. Top graph shows the integrated water blend fluxes at 15.17 μm , the middle graph at 17.22 μm and the bottom at 29.85 μm . The circles represent water detections whereas the triangles represent upper limits for water detections. Sources marked in red indicate the objects which show a significant degree of crystallization. Stellar luminosities that are known for some of these sources are shown in the figure.

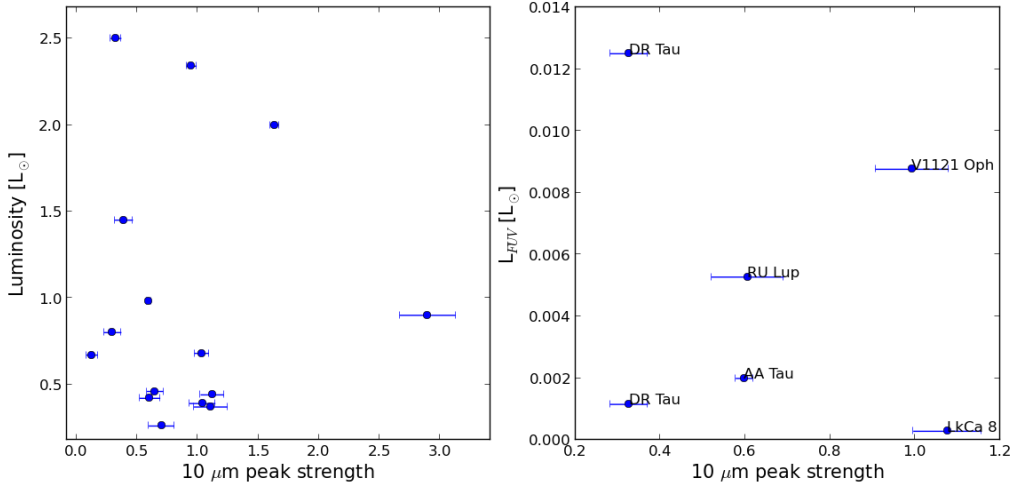


Figure 5: Left: Luminosity versus the peak strength of the $10 \mu\text{m}$ silicate feature; Right: FUV luminosity versus the peak strength of the $10 \mu\text{m}$ silicate feature, the possible explanation for the fact that DR Tau has two different values, is that one of the observations took place during an active phase of this source. The values for the FUV luminosities are obtained from Yang et al. (2012).

4 Modeling using ProDiMo

The code used for analysis is ProDiMo (Woitke et al., 2009). This is a code that simulates the 2D structure of protoplanetary disks. It calculates the detailed physical and chemical structure of disks taking into account the complex nature of radiative transfer and chemical processes. A large amount of parameters are implemented into the code which allow to vary the geometrical structure, properties of gas and dust, properties of the central star etc. Detailed analysis of a large range of emission lines is also possible. Therefore this model presents an ideal tool to study detailed effects of various physical changes.

4.1 The standard model

The standard model will be the basis for the modeling analysis in this thesis. It is the same as used by Antonellini et al. (2015b, under revision). In this model, the central star was chosen to be a typical T Tauri star of spectral type K with a mass of $0.8 M_{\odot}$ and a surface temperature of 4400 K. The distance to this disk is set to 140 pc. In addition to an assumed FUV excess of 1% of the stellar radiation, X-ray irradiation from the star is also taken into account. This star is surrounded by a flared disk with a mass of $0.01 M_{\odot}$ and a minimum dust grain size of $0.05 \mu\text{m}$. This model takes into account dust settling whereas viscous heating is ignored. An overview of the parameters for the central star and the disk is shown in Table 3.

Table 3: List of parameters used in the standard model

Stellar and radiative parameters	Symbol	Value
Photospheric temperature	T_{eff}	4400 [K]
Stellar mass	M_{*}	$0.8 [M_{\odot}]$
Stellar luminosity	L_{*}	$0.7 [L_{\odot}]$
FUV excess	L_{UV}/L_{*}	0.01
UV powerlaw exponent	p_{UV}	0.2
X-ray luminosity	L_{X}	$10^{30} [\text{erg s}^{-1}]$
X-ray minimum energy	$E_{\min, \text{X}}$	0.1 [keV]
X-ray temperature	T_{X}	$10^7 [\text{K}]$
Disk parameters		
Disk mass	M_{gas}	$0.01 [M_{\odot}]$
Outer radius	R_{out}	300 [AU]
Inner radius	R_{in}	0.1 [AU]
Reference radius	R_0	0.1 [AU]
Scale height at reference radius	H_0	$3.5 \cdot 10^{-3} [\text{AU}]$
Tapering-off radius	R_{taper}	200 [AU]
Power law index surface density	ϵ	1.0
Minimum dust size	a_{\min}	$0.05 [\mu\text{m}]$
Distance	d	140 pc

The vertical structure of the disk is described by the scale height H (Antonellini et al., 2015b, under revision), which describes the rate at which the pressure falls off in the vertical direction at a radius r . The parameters that affect the structure at most are the flaring parameter β which sets the degree of flaring and the tapering off radius which sets the location at which the density falloff changes from a power law to an exponential decay. The scale height is parametrized as

$$H(r) = H_0 \left(\frac{r}{R_0} \right)^{\beta} \quad (9)$$

where R_0 is the reference radius at which the scale height has a value of value of H_0 . The surface density Σ of the disk (Antonellini et al., 2015b, under revision), changes as a function of radius. The shape of the density distribution is set by the surface density power law index ϵ and the γ exponent that regulates the exponential decrease of the density profile. The first term with the ϵ exponent dominates the inner

parts of the disk whereas the outer part of the disk is dominated by the last term. The expression for the surface density is given by

$$\Sigma(r) = \Sigma_0 \left(\frac{r}{R_0} \right)^{-\epsilon} \exp \left[- \left(\frac{r}{R_{\text{taper}}} \right)^{2-\gamma} \right] \quad (10)$$

where R_{taper} is tapering off radius which sets the location at which the density falloff changes from a power law to an exponential decay. The density distribution (Antonellini et al., 2015b, under revision) is both a function of radius and height; it decreases exponentially with height following the scale height

$$\rho(r, z) = \frac{\Sigma(r)}{\sqrt{2\pi H}} \exp \left(-\frac{z^2}{2H^2} \right) \quad (11)$$

Line luminosities in each cell in the model are evaluated through the following expression

$$L_{\text{cell}} = n_u A_{ul} h\nu_{ul} p_{\text{esc}} e^{-\tau_{\text{dust}}} dV \quad (12)$$

in which n_u represents the number density of the particular upper state, A_{ul} represents the probability per unit time for spontaneous emission from the u to l level, $h\nu_{ul}$ is the expression for the energy of the emitted photon, p_{esc} is the escape probability that expresses the probability that the emitting photon escapes from the volume without being reabsorbed and the $\exp(-\tau_{\text{dust}})$ term includes decreases in flux as a consequence of the opacity of the dust. Average quantities of the emitting region in which 15-85 % of the line flux is emitted are determined by the model through radial and vertical integration over this region

$$\langle X \rangle = \frac{\int_{r_{in}}^{r_{out}} \int_{z_{low}}^{z_{high}} X n_{\text{gas}} 2\pi r dr dz}{\int_{r_{in}}^{r_{out}} \int_{z_{low}}^{z_{high}} n_{\text{gas}} 2\pi r dr dz} \quad (13)$$

where n_{gas} is the gas volume density. In this study the gas temperature distribution is of great importance since it sets the extent of regions that host the conditions for mid-IR line emissions. The gas temperature distribution of the standard model within the disk is shown in Fig. 6. Gas temperatures range from 5000 K in the uppermost surface layers to tens of kelvin in the mid-plane regions. The particle density distribution within the standard models disk is shown in Fig. 6 which shows the radial and vertical decrease in density. Densities range from 10^3 cm^{-3} in the uppermost layers up to 10^{15} cm^{-3} in the innermost regions.

In the following sections, the effect of changing dust and gas properties on mid-IR water emission and the peak strength of the silicate feature will be investigated. Effects on the dust opacity, gas temperature structure, dust temperature structure and average grain size distribution will be viewed. In these series, the water line blends at 15.17, 17.22 and 29.85 μm are investigated. In addition a closer look will be taken on the properties of the line emitting regions. The 17.22 μm line emitting region is not analyzed in detail, since we only want to explore the effect on high and low excitation lines that is covered by the 15.17 and 29.85 μm emission lines. Since emission lines within the blends are separated by small differences, we expect the behavior of the emission lines being studied to be similar to the behavior of the blends in question.

4.2 Variation of dust properties

In order to understand how certain properties of dust affect the mid-IR water emission together with the peak strength of the 10 μm silicate feature, existing model series (Antonellini et al., 2015b, under revision) for a range of parameters will be used. The influence of the maximum dust grain size and the effect of different power law indices of the dust size distribution will be studied.

4.2.1 Variation of maximum grain size

In order to get a better understanding of the structure of protoplanetary disks as they evolve over time, we simulate the effect of dust grain growth. As stated in the introduction, dust particles will evolve in size over time as a consequence of various processes such as coagulation and dust settling. Therefore the model has been calculated for different maximum grain radii of dust grains: $a_{\text{max}} = 2.5 \cdot 10^2, 4.0 \cdot 10^2,$

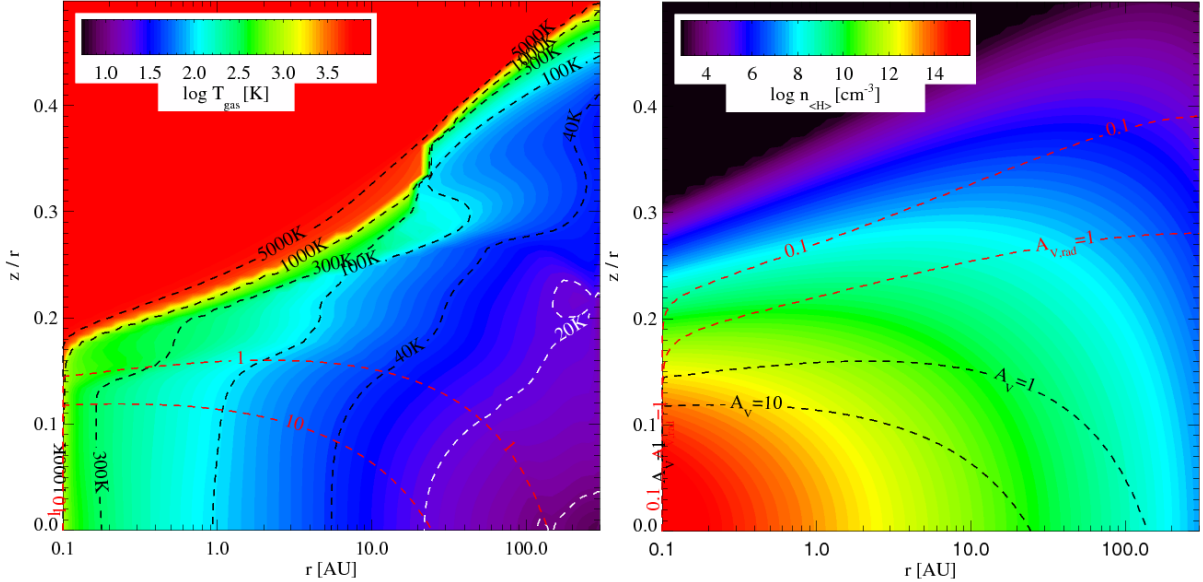


Figure 6: The gas temperature distribution within the standard model in which the red dashed lines represent the visual extinction A_V of 1 and 10 (left); the particle density structure in which the black dashed lines represent the visual extinction A_V of 1 and 10 and the red dashed lines show the radial visual extinction $A_{V,rad}$ of 0.1 and 1 (right)

$5.0 \cdot 10^2$, $7.0 \cdot 10^2$, 10^3 , $2.0 \cdot 10^2$, $5.0 \cdot 10^3$, 10^4 and 10^5 μm . Mid-IR Spectra having a resolution of 600 in the Spitzer range for all of these values are acquired from the model. Besides, this model constructs an SED corresponding to each spectrum. These spectra and their corresponding SED are shown in Appendix A in which the silicate feature is prominently visible.

In order to analyze the silicate feature and the water blends, the modeled SED for each spectrum is invoked. The SED solely represents the continuum, whereas the spectrum is the SED added with lines on top having a resolution of 600. This addition requires additional wavelength points at each line wavelength. Line fluxes are added as a peak with the corresponding height. Spectra are then obtained by a convolution with a resolution of 600. Further analysis requires the flux of the SED to be evaluated at the same wavelengths as the spectrum. This is achieved by interpolation of the SED using cubic spline interpolation² for the wavelengths of the spectrum. Peak strengths of the $10 \mu\text{m}$ silicate feature are obtained in the same manner as explained in the previous chapter. To study the water blends, the SED is subtracted from the spectrum resulting in the net flux contribution of the water blends. Gaussian functions are fitted to the blends to enable the calculation of integrated blend fluxes. This is achieved using a Gaussian function with undetermined parameters for the amplitude a , mean μ , and standard deviation σ

$$F_{\text{blend}} = a \cdot e^{-\frac{(\lambda - \mu)^2}{2\sigma^2}} \quad (14)$$

The region where the blend fit is calculated is carefully chosen in order to avoid the contribution of other blends. These are, 15.1400-15.1900 μm for the $15.17 \mu\text{m}$ blend, 17.1855-17.2512 for the $17.22 \mu\text{m}$ blend and 29.7431-29.9684 μm for the $29.85 \mu\text{m}$ blend. Optimization of these undetermined parameters³ result in the fit. This optimization required the input of initial guesses of the parameters. These are chosen to be, $a = 1$ and the values for μ and σ are calculated for the particular region using the python modules numpy.mean and numpy.std. These blends together with the corresponding fitted Gaussian functions are shown in Fig. 7 where the fits are plotted for a wider frequency range to show the full contribution of the blend. Total fluxes of the blends are determined by integrating the fitted profiles⁴.

Integrated line fluxes together with the peak strength of the silicate feature are shown in Fig. 8 and listed in Table 4. There is a clear correlation between the peak strength of the silicate feature and the integrated water blend fluxes. As the size of the largest grains increase, water blend fluxes are seen to

²For the spline interpolation the `scipy.interpolate.interp1d` module is used

³For the optimization of the fit, the `scipy.optimize.curve_fit` module is used

⁴Integration is carried out using the `scipy.integrate.quad` module

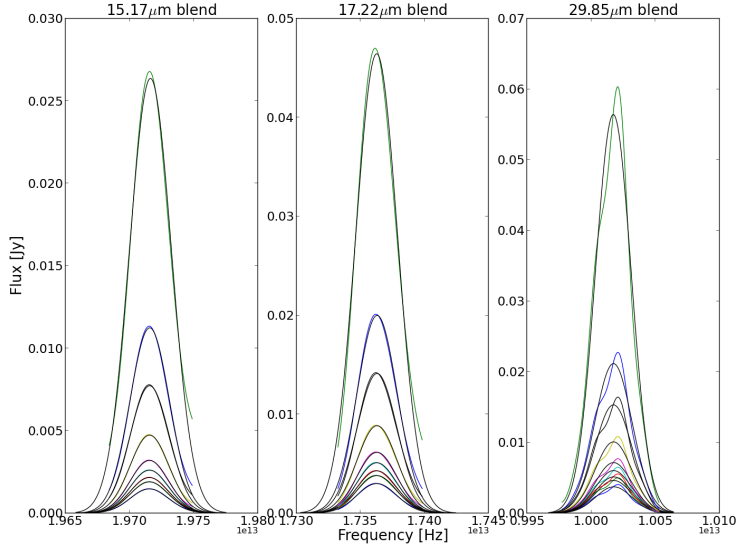


Figure 7: Water blends with their corresponding Gaussian fitted profiles, each color represents a blend corresponding to a spectrum of a particular maximum grain size. Maximum grain sizes decrease from top to bottom. The corresponding Gaussian fitted profiles are shown in black.

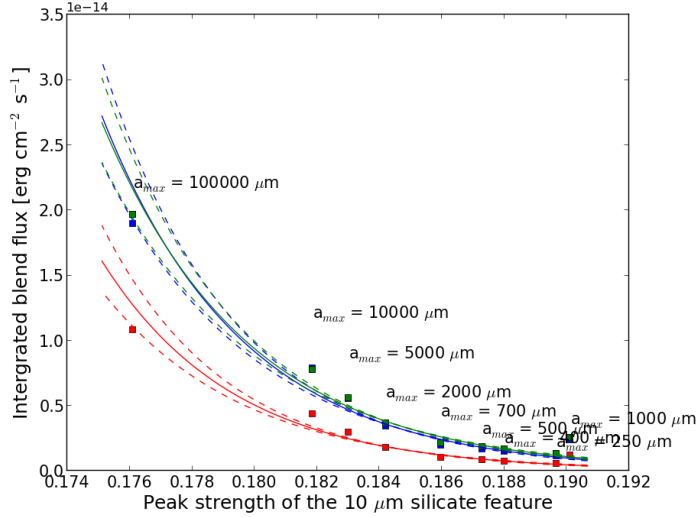


Figure 8: Water blend fluxes versus the peak strength of the $10 \mu\text{m}$ silicate feature for all maximum grain radii. Red indicates the $15.17 \mu\text{m}$ blend, blue the $17.22 \mu\text{m}$ blend and green the $29.85 \mu\text{m}$ blend. Squares represent the data points, solid lines the fit and dotted lines the 1σ confidence interval of the fit

increase. In order to interpret these results, a closer look is needed on how the physical conditions within the disk are affected. An important aspect is how the dust opacity changes with the maximum grain size and what its implications are. In Fig. 9, the dust continuum opacity is given for maximum grain radii of $2.5 \cdot 10^2 \mu\text{m}$ and $10^5 \mu\text{m}$. For $\lambda < 100 \mu\text{m}$ the opacity decreases up to two orders of magnitude whereas for $\lambda > 10^3 \mu\text{m}$ the opacity increases up to two orders of magnitudes while increasing maximum grain radii from $2.5 \cdot 10^2 \mu\text{m}$ to $10^5 \mu\text{m}$. On account of the fact that the dust mass in this model is kept constant, the amount of small grains declines when approaching larger maximum grain sizes. This is because large grains dominate the mass budget of dust. As the surface area of dust grains is dominated by the small grains, this is the main explanation for the decrease in opacity at small wavelengths. Effects

Table 4: Results for different maximum dust grain radii.

a_{\max} μm	15.17 μm blend flux [erg $\text{cm}^{-2} \text{s}^{-1}$]	17.22 μm blend flux [erg $\text{cm}^{-2} \text{s}^{-1}$]	29.85 μm blend flux [erg $\text{cm}^{-2} \text{s}^{-1}$]	peak strength of the 10 μm silicate feature
250	$5.58 \cdot 10^{-16}$	$1.16 \cdot 10^{-15}$	$1.32 \cdot 10^{-15}$	0.190
400	$7.20 \cdot 10^{-16}$	$1.47 \cdot 10^{-15}$	$1.64 \cdot 10^{-15}$	0.188
500	$8.21 \cdot 10^{-16}$	$1.66 \cdot 10^{-15}$	$1.83 \cdot 10^{-15}$	0.187
700	$9.92 \cdot 10^{-16}$	$1.98 \cdot 10^{-15}$	$2.15 \cdot 10^{-15}$	0.186
10^3	$1.22 \cdot 10^{-15}$	$2.39 \cdot 10^{-15}$	$2.57 \cdot 10^{-15}$	0.190
$2 \cdot 10^3$	$1.81 \cdot 10^{-15}$	$3.45 \cdot 10^{-15}$	$3.64 \cdot 10^{-15}$	0.184
$5 \cdot 10^3$	$2.98 \cdot 10^{-15}$	$5.54 \cdot 10^{-15}$	$5.60 \cdot 10^{-15}$	0.183
10^4	$4.35 \cdot 10^{-15}$	$7.87 \cdot 10^{-15}$	$7.75 \cdot 10^{-15}$	0.182
10^5	$1.08 \cdot 10^{-14}$	$1.89 \cdot 10^{-14}$	$1.97 \cdot 10^{-14}$	0.176

of the changing opacity are seen in the modeled spectra (Appendix A) in which the dust continuum decreases for larger maximum grain sizes. At lower opacities the disk will become more transparent,

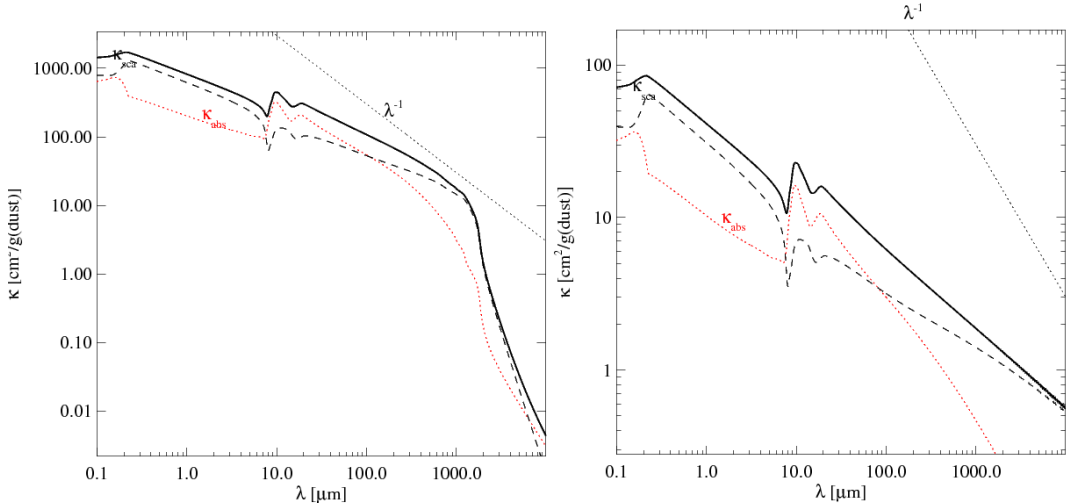


Figure 9: Dust continuum opacities for $a_{\max} = 250 \mu\text{m}$ (left), and $a_{\max} = 100000 \mu\text{m}$ (right). The red line indicates the contribution to opacity by absorption and the black dashed line represents the contribution of scattering. The black solid line represents the sum on the two contributions. The silicate features in the opacity are the bumps at 10 μm and 20 μm .

hence the intense radiation field from the central star will penetrate to larger depths, vertically as well as radially covering a larger region. The region containing water ice that was previously shielded is now partly exposed to stellar radiation. In addition to the region containing water vapor being radially and vertically more extended, the abundance of water in the gas phase is enhanced; this effect can be seen in Fig. 11. As the maximum grain size increases, the gas temperature distribution within the disk changes, deeper regions e.g. those that are closer to the mid-plane and located at larger radii become warmer. Comparison between the distribution of the gas temperature within the disk for the smallest and largest maximum grain size is shown in Fig. 10. In this plot, the effect on the gas temperature distribution becomes visible, where the temperature is significantly enhanced radially as well as vertically. Radial and vertical gas temperature gradients are seen to change; these decrease with increasing grain sizes. Fig. 10 shows the downwards displacement of the A_V extinction lines, showing the increased transparency of the disk. When comparing gas temperatures to dust temperatures (Fig. 10), it is seen that gas temperatures are significantly higher than those of the dust in the uppermost surface layers. So, gas and dust are kinetically uncoupled, whereas in the lower regions, gas and dust temperatures are equal. This effect was explained by Kamp and Dullemond (2004). The fact that warmer regions extend further out has profound consequences on the emission characteristics of water. Gas temperature

gradients become shallower in the region from which the mid-IR water lines originate. Detailed analysis of the line emitting regions $\text{o-H}_2\text{O } 15.19 \mu\text{m}$ and $\text{o-H}_2\text{O } 29.85 \mu\text{m}$ is shown in Fig. 11. In addition to this plot, some properties of the emitting regions are listed in Table 5.

From this we can draw a number of conclusions. First of all it is seen that for any case, the emission region of the $\text{o-H}_2\text{O } 29.85 \mu\text{m}$ line traces regions further out in the disk and is more extended in comparison to the $\text{o-H}_2\text{O } 15.19 \mu\text{m}$ emission region. This can be understood through the fact that temperatures decrease radially, so the conditions at larger radii are favorable for lower excitation transitions. This is in agreement with Meijerink et al. (2009), who suggest that transitions in the mid-IR range with lower excitation energies trace larger radii of the disk. As the maximum grain radius increases, the emitting regions increase in radial extension and migrate upwards. The area of the $\text{o-H}_2\text{O } 15.19 \mu\text{m}$ emission region increases by a factor of 9.8 and the $\text{o-H}_2\text{O } 29.85 \mu\text{m}$ emission region increases by a factor of 8.1 in area while increasing the maximum grain size from $2.5 \cdot 10^2 \mu\text{m}$ to $10^5 \mu\text{m}$. This is the result of the decrease in the gas temperature gradient. Lower average gas and dust temperatures are the result of an increased radial extension of these emitting regions. The decrease in average density of water within the emission regions is explained by means of the upper displacement, as the density decreases in the vertical direction.

Table 5: Properties of the water line emission regions

Line at $a_{max} = 250 \mu\text{m}$	$\text{o-H}_2\text{O } 15.18890 \mu\text{m}$	$\text{o-H}_2\text{O } 29.85089 \mu\text{m}$
Average $\text{o-H}_2\text{O}$ density [cm^{-3}]	$6.47 \cdot 10^{10}$	$2.16 \cdot 10^{10}$
Radial extension [AU]	$0.101 - 0.109$	$0.110 - 0.238$
Vertical extension [AU]	$0.015 - 0.014$	$0.026 - 0.022$
Gas Temperature [K]	769.35	319.27
Dust Temperature [K]	769.30	319.25
<hr/>		
Line at $a_{max} = 10^5 \mu\text{m}$		
Average $\text{o-H}_2\text{O}$ density [cm^{-3}]	$3.85 \cdot 10^{10}$	$1.45 \cdot 10^9$
Radial extension [AU]	$0.102 - 0.164$	$0.174 - 0.625$
Vertical extension [AU]	$0.016 - 0.015$	$0.044 - 0.038$
Gas Temperature [K]	461.47	212.79
Dust Temperature [K]	460.24	208.08

The major effect for the increase in the line fluxes is a combination of the decrease of the line optical depth in the emitting region together with the increased radial extension of the emitting regions. Combining these effects together with the analysis of the water blends, it becomes clear why the flux of mid-IR water emission lines increase with increasing maximum grain size. The opposite behavior in the trend for a maximum grain size of $1000 \mu\text{m}$ remains unclear.

For an explanation of the change in the peak strength of the $10 \mu\text{m}$ silicate feature as a consequence of increasing dust grains sizes, the distribution of the dust temperature is considered. The radial and vertical dust temperature gradient is not showing any significant changes. As a result of the increased transparency for larger maximum grain sizes, the optically thick dust layers displace downwards. This results in a downwards migration of the region from which the $10 \mu\text{m}$ emission originates, as the $10 \mu\text{m}$ emission originates from the layers just above the $A_V = 1$ line. Detailed analysis is made on the $10 \mu\text{m}$ emission region. For all maximum grain sizes, the extension of the $10 \mu\text{m}$ emitting region is determined from the model in which radially and vertically 15-85% of the $10 \mu\text{m}$ flux is emitted. The result is shown in Fig.12. The location of the $10 \mu\text{m}$ emission region is overall in good agreement with the relation $R_{10} = 0.35\text{AU}(L_*/L_\odot)^{0.56}$ for the silicate emission zone that was found by Kessler-Silacci et al. (2007), this radial location is shown in Fig. 12. Our result resembles a downward displacement of the emitting region, as is observed in the dust temperature distribution. As the region propagates deeper into the disk, no significant changes are observed in its vertical extension. However, it is interesting to notice that the radial extent of the emitting region decreases with increasing grain size. The decreased radial extension of the $10 \mu\text{m}$ emission region is explained by an increase in the dust temperature gradient that extends the region that hosts the conditions for the $10 \mu\text{m}$ silicate emission feature. This increase is the

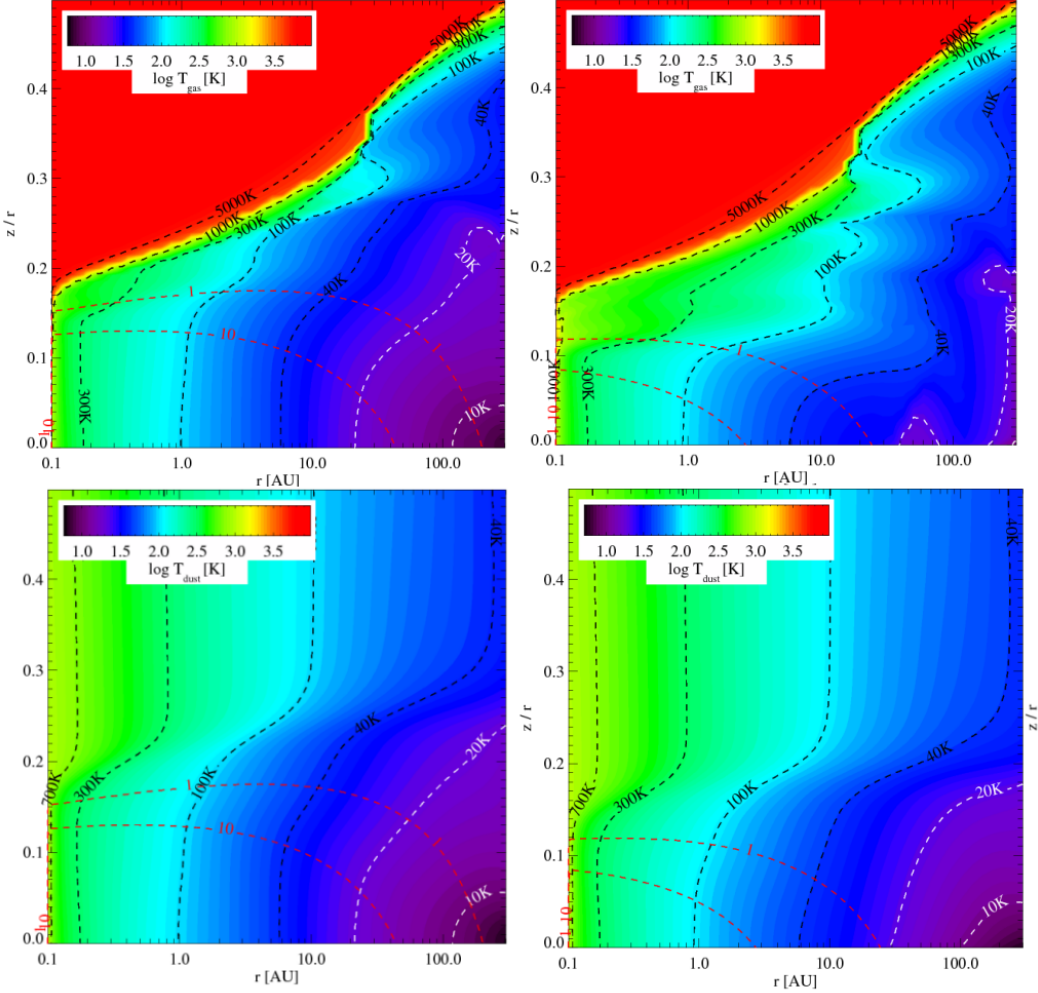


Figure 10: Left column represents $a_{max} = 250 \mu\text{m}$; the right column represents $a_{max} = 10^5 \mu\text{m}$. The top row indicates the distribution of the gas temperature where the black dashed lines indicate the gas temperature, the bottom row indicates the distribution of the dust temperature where the black dashed lines indicate the dust temperature. The red lines represent the visual extinction A_V of 1 and 10 respectively.

result of the downward displacement of the emission region. Decreases of the peak strength of the $10 \mu\text{m}$ silicate feature are ascribed to a combination of decreased grain sizes and lower radial extensions of this emitting region. Decreases due to smaller dust grains are explained by the fact that the $10 \mu\text{m}$ feature only traces grains that are smaller than a few microns (Natta et al., 2007) and hence the strength of the $10 \mu\text{m}$ silicate feature is inversely correlated to the dust grain size. The results above give a clear indication for the inverse trend that is observed between the water blend fluxes and the peak strength of the $10 \mu\text{m}$ silicate feature.

In order to quantify the correlation between the peak strength of the silicate feature and the mid-IR water emission, a fit is made to the trend in Fig 8. This is achieved by transforming the integrated line flux data into log-space followed by calculating a linear fit to this trend using the python module `scipy.optimize.curve_fit`. Together with the fit, 1σ confidence intervals in which the fit lies are evaluated using the uncertainties in the parameters of the fit provided by this module. For all three emission lines a separate fit is made. In evaluating this fit, the values for a maximum grain size of $1000 \mu\text{m}$ are omitted. Subsequently, the fit is transformed back into linear coordinates.

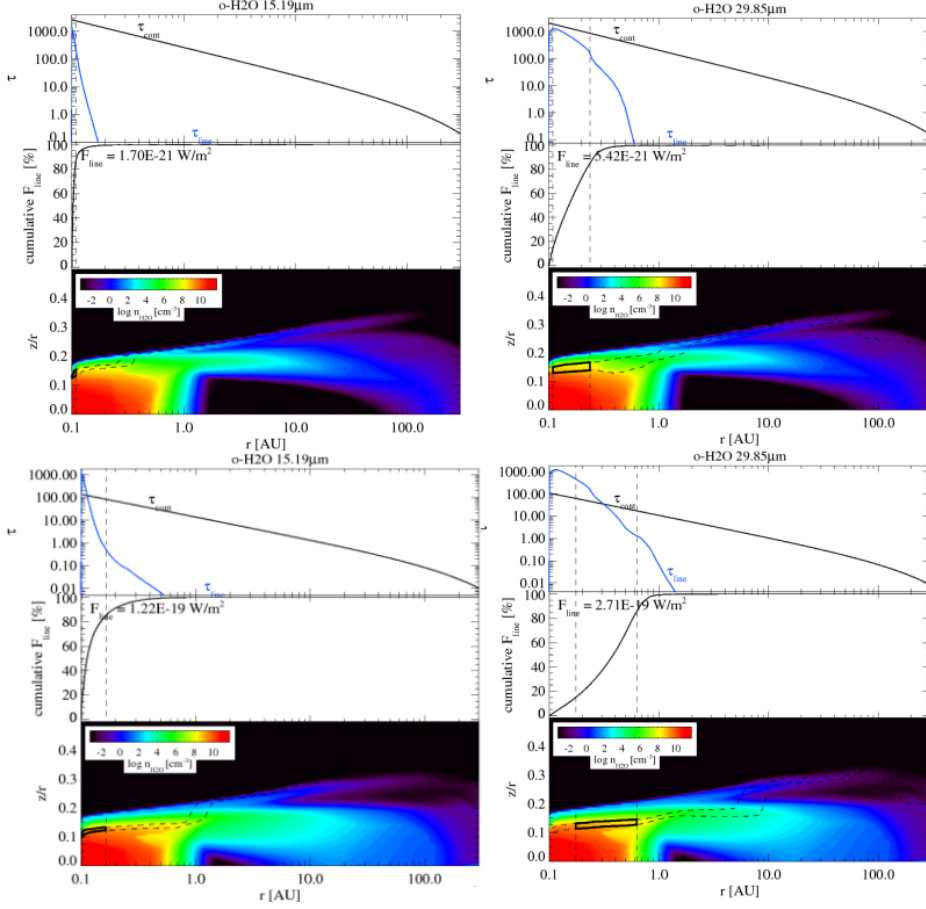


Figure 11: Analysis of the lines o-H₂O 15.19 μm left column and o-H₂O 29.85 μm right column. Top row indicates the results for a maximum grain size of 250 μm , the bottom row shows the results for a maximum grain size of 10⁵ μm . Each figure is represented by an opacity plot that contains information about the continuum and line opacity, on top, the cumulative line flux, middle, and a plot containing the distribution of water and the region (black box) where 15–85% of line emission originates from. The grey dashed lines indicate the radial and vertical extend of the emitting region in all the plots.

The expressions for the correlations are given by

$$F_{\text{o-H}_2\text{O } 15.19\mu\text{m}} = 10^{-23} \cdot e^{-236.63 \cdot S_{10\mu\text{m}} + 62.64} \text{ [erg cm}^{-2} \text{ s}^{-1}] \quad (15)$$

$$F_{\text{o-H}_2\text{O } 17.23\mu\text{m}} = 10^{-23} \cdot e^{-222.55 \cdot S_{10\mu\text{m}} + 60.69} \text{ [erg cm}^{-2} \text{ s}^{-1}] \quad (16)$$

$$F_{\text{o-H}_2\text{O } 29.85\mu\text{m}} = 10^{-23} \cdot e^{-213.85 \cdot S_{10\mu\text{m}} + 59.15} \text{ [erg cm}^{-2} \text{ s}^{-1}] \quad (17)$$

These fits are shown Fig 8. We find that different water emission lines that we study have different dependencies on the peak strength of the silicate feature. The o-H₂O 15.19 μm emission line has the strongest dependence on the peak strength of the silicate feature. The explanation for this is the combination of the strong effect of the emitting area together with the fact that this line is more energetic than the other ones, enhancing the blend flux. The o-H₂O 29.85 μm emission line has the weakest dependence on the peak flux of the silicate feature. Therefore it appears that shorter emission lines are stronger related to the peak strength of the silicate feature. With increasing peak strength of the silicate feature, the qualitative behavior of the correlation of all three lines is the same as the integrated water blend fluxes diminish.

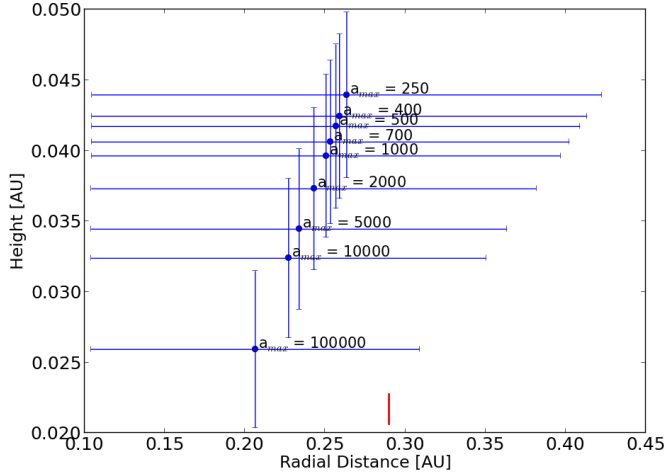


Figure 12: The extent and position of the $10\mu\text{m}$ emission region from which 15–85% of the $10\mu\text{m}$ emission arises. The red bar indicates the radial location of the $10\mu\text{m}$ emission region according to Kessler-Silacci et al. (2007), this only indicates the radial positions and contains no information about the vertical extent.

4.2.2 Variation of the power-law index of the dust size distribution

Effects of different dust size distributions on the structure and emission of disks will be studied. As mentioned in the section about dust, the dust size distribution is represented by a power law $n(a) \sim a^{-a_{\text{pow}}}$ that indicates how many grains of a certain size represent the overall population of dust grains. This distribution depends on the age of the protoplanetary disk in which dust size particles grow in size over time. Eventually the amount of small dust grains decreases reducing the power law index. We explore a range of power law indices (a_{pow}): 2.0, 2.5, 3.0, 3.5, 4.0 and 4.5. For each power law index, a mid-IR spectrum in the Spitzer range with a resolution of 600 is calculated by the model as previously described. Spectra for the range of power law indices being investigated are shown in Appendix B. The spectra show the presence of the $10\mu\text{m}$ silicate feature. These modeled spectra will be analyzed in the same fashion as described in the previous section. Gaussian fits for the water blends investigated here and the blends themselves are shown in Fig. 13. The same blend widths as above are used. Integrated water blend fluxes obtained from these blends together with peak strengths of the $10\mu\text{m}$ silicate feature are shown in Fig. 14, listed in Table. 6. In this figure, values for power law indices 2.0 and 2.5 were omitted for the reason that for these cases the silicate feature is present in absorption.

Table 6: Results for different power law indices

a_{pow}	$15.17\mu\text{m}$ blend flux [$\text{erg cm}^{-2}\text{s}^{-1}$]	$17.22\mu\text{m}$ blend flux [$\text{erg cm}^{-2}\text{s}^{-1}$]	$29.85\mu\text{m}$ blend flux [$\text{erg cm}^{-2}\text{s}^{-1}$]	peak strength of the $10\mu\text{m}$ silicate feature
2.0	$2.86 \cdot 10^{-14}$	$4.36 \cdot 10^{-14}$	$6.43 \cdot 10^{-14}$...
2.5	$2.20 \cdot 10^{-14}$	$3.51 \cdot 10^{-14}$	$5.69 \cdot 10^{-14}$...
3.0	$1.08 \cdot 10^{-14}$	$1.93 \cdot 10^{-14}$	$2.48 \cdot 10^{-14}$	0.05
3.5	$1.22 \cdot 10^{-15}$	$2.39 \cdot 10^{-15}$	$2.57 \cdot 10^{-15}$	0.19
4.0	$2.43 \cdot 10^{-16}$	$5.13 \cdot 10^{-16}$	$6.02 \cdot 10^{-16}$	0.37
4.5	$2.55 \cdot 10^{-16}$	$5.66 \cdot 10^{-16}$	$5.31 \cdot 10^{-16}$	0.53

Our findings show an anti-correlation between the integrated water line emission and the peak strength of the $10\mu\text{m}$ silicate feature with increasing power law index. A change in the power law index significantly alters the structure of the disk. We note that dust opacities strongly depend on the power law index.

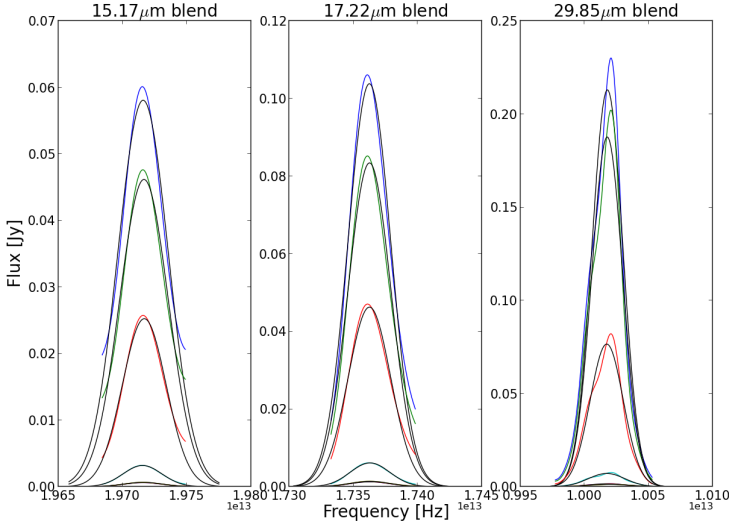


Figure 13: Water line blends with their corresponding Gaussian fitted profiles. Each color represents a blend corresponding to a spectrum of a particular power law index. The power law index increases from top to bottom. The corresponding Gaussian fitted profiles are shown in black.

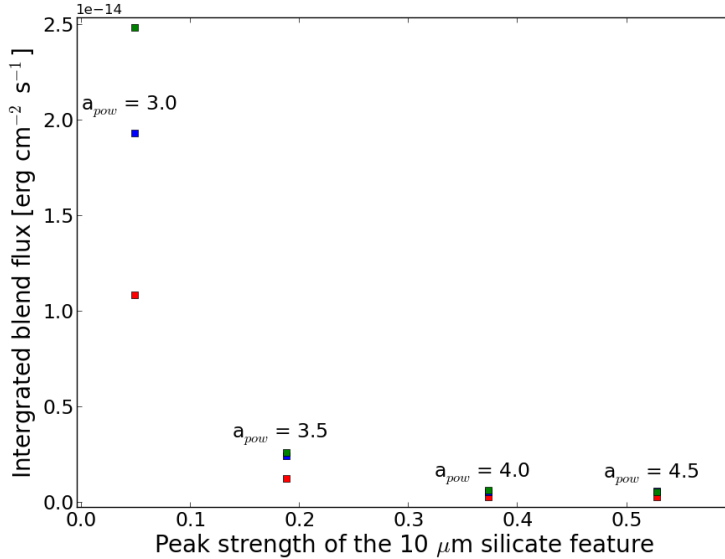


Figure 14: Water blend fluxes versus the peak strength of the $10 \mu\text{m}$ silicate feature. The values for the power laws 3.0, 3.5, 4.0 and 4.5 are shown, red indicates the $15.17 \mu\text{m}$ blend, blue the $17.22 \mu\text{m}$ blend and green the $29.85 \mu\text{m}$ blend

Dust opacities for power law indices 2.0 and 4.5 are shown in Fig. 15. The grain size distribution with an index of 2.0 features the population with the least amount of small grains in this series. For the 2.0 power law index, we note that the opacity is almost constant for $\lambda < \sim 1000 \mu\text{m}$. No traces of the silicate feature are visible in the dust opacity for the 2.0 power law index. This can be understood by the fact that the $10 \mu\text{m}$ silicate feature is produced only by grains that are smaller than a few microns (Natta et al., 2007). With increasing power-law indices, the contribution of small grains to the population of dust grains increases. This results in an increase in the dust opacity together with the appearance of the $10 \mu\text{m}$ silicate feature. Strong increases of dust opacities for $\lambda < 10 \mu\text{m}$ and decreases at $\lambda > 100 \mu\text{m}$ for increasing power law indices indicates that the opacity indeed is dominated by small grains. The extinction within the disk increases strongly with increasing power law indices, as seen in Fig. 16 by the

upwards displacement of the A_V extinction lines. These large changes in opacity will affect the temper-

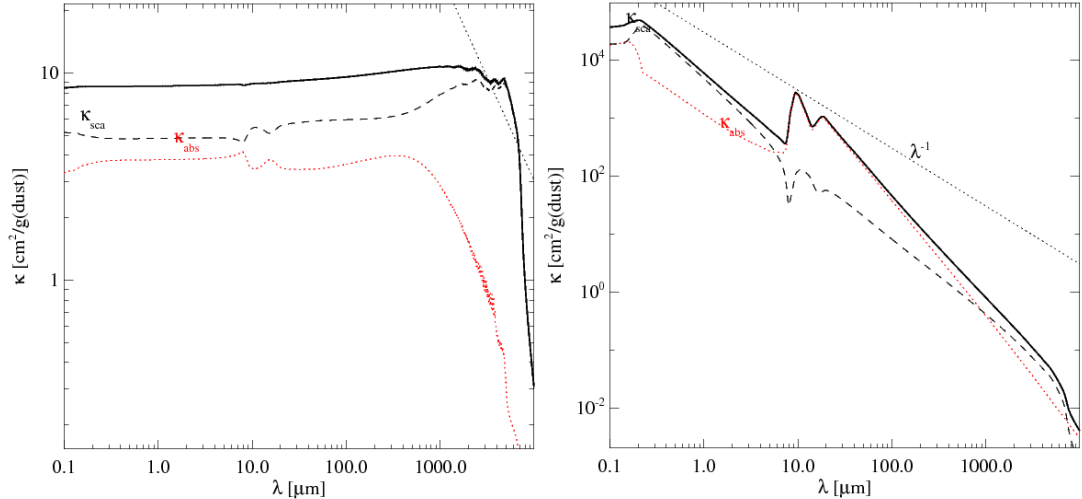


Figure 15: Dust continuum opacities for $a_{pow} = 2.0$ (left), and $a_{pow} = 4.5$ (right). The red dotted line indicates the contribution to the opacity by absorption, the black dashed line represents the contribution of scattering and the black solid line represents the sum of these two contributions.

ature distribution within the disk. Temperature distributions of gas and dust are shown in Fig. 16 for power law indices of 2.0 and 4.5. Gas and dust temperature distributions are strongly altered with increasing power law index. Towards larger power law indices, inner regions of the disk e.g. radially as well as vertically become colder. This is the effect of an increased amount of shielding provided by the small grains. The gas temperature gradient is strongly affected by the power law index: It strongly increases with increasing power law index. This decrease in temperature within the disk will affect the abundance of water vapor. Since the region in which water freezes out increases in vertical and radial extension, the water vapor abundances will decrease. This effect is seen in Fig. 17. Significant changes in conditions within the disk affects the emission of mid-IR water lines. Analysis of the emission lines o-H₂O 15.19 μm and o-H₂O 29.85 μm are shown in Fig. 17. Besides, a range of properties of the emitting line regions are listed in Table 7. Both emission regions are affected and show similar behavior. These emission regions advance downwards and migrate to smaller radii with increasing power law indices. In addition, these regions show a strong decrease in total radial extension. The fact that the radial extension of the emitting regions strongly decreases, can be explained by means of increases of gas temperature gradients which sets the extent of regions that satisfy the conditions for the emission of these lines. Downward migration of the mid-IR emission regions result in an increase in line optical depths within the regions as a consequence of larger densities being encountered (Fig. 17). The extent of the o-H₂O 15.19 μm emission region is affected the most and decreases in area by a factor of 89 whereas the o-H₂O 29.85 μm emission area decreases only by a factor of 4.91. We find that for large power law indices, integrated line fluxes of the o-H₂O 15.19 μm and o-H₂O 17.22 μm lines show an opposite behavior to the overall trend (Fig. 13). Increasing the power law index from 4.0 to 4.5, the integrated blend flux of the o-H₂O 15.19 μm line increases with 5% and the integrated blend flux of o-H₂O 17.22 μm increases by 10%. We expect in principle the overall trend to continue, in which the water line blend fluxes decrease with increasing peak strengths of the 10 μm silicate feature. Uncertainties can be of the order of a few-10 % due to differences in the numerical accuracy, which depends on how well the water emission region and temperature gradients are resolved. Therefore this opposite behavior is ascribed to numerical uncertainties in the model. To summarize, the combined effect of the increased line optical depths and the decrease of the radial extension of the emitting regions is responsible for the strong decreases in water line fluxes with increasing power-law indices.

In addition to significant changes in the gas temperature distribution, the distribution of the dust temperature and the average grain size distribution are also affected by the power law index. As a consequence

Table 7: Properties of the line emitting regions

Line at $a_{\text{pow}} = 2.0$	$\text{o-H}_2\text{O } 15.18890 \mu\text{m}$	$\text{o-H}_2\text{O } 29.85089 \mu\text{m}$
Average o-H ₂ O density [cm ⁻³]	$8.46 \cdot 10^9$	$2.12 \cdot 10^9$
Radial extension [AU]	$0.113 - 0.294$	$0.192 - 0.494$
Vertical extension [AU]	$0.020 - 0.017$	$0.033 - 0.027$
Gas Temperature [K]	336.50	279.51
Dust Temperature [K]	299.61	213.24
<hr/>		
Line at $a_{\text{pow}} = 4.5$		
Average o-H ₂ O density [cm ⁻³]	$5.69 \cdot 10^{10}$	$2.44 \cdot 10^{10}$
Radial extension [AU]	$0.101 - 0.105$	$0.106 - 0.231$
Vertical extension [AU]	$0.016 - 0.014$	$0.026 - 0.022$
Gas Temperature [K]	984.15	342.04
Dust Temperature [K]	984.08	342.04

of large increases in the dust opacity, optically thick dust layers displace upwards as can be seen in Fig. 16 in which the $A_V = 1$ extinction line significantly moves upward with increasing power law index. Therefore the region from which the $10 \mu\text{m}$ emission originates migrates upwards. This upwards displacement results in a decrease of the dust temperature gradient within the $10 \mu\text{m}$ silicate emission region. For all power law indices, spatial properties of the $10 \mu\text{m}$ emission region are determined from the model in which radially and vertically 15–85% of the $10 \mu\text{m}$ flux is emitted. The location and extent of the $10 \mu\text{m}$ emitting region is shown in Fig. 18. Again, locations of the $10 \mu\text{m}$ emission zone are in good agreement with the location of the silicate emission zone found by Kessler-Silacci et al. (2007). The $10 \mu\text{m}$ emission region according to their relation for the star in this model is shown in Fig. 18. As mentioned above, for power law indices 2.0 and 2.5, the silicate feature is seen as absorption in the spectrum. In order to explain this, a closer look is needed on the distribution of average grain sizes within the disk (Fig. 16). Large gradients in the average grain size distribution within the disk for power-law indices 2.0 and 2.5 are observed, in which average grain sizes decrease towards upper regions. Average grain sizes of tenths of microns are found in the $10 \mu\text{m}$ emission region. As these grains do not produce a silicate feature, a possible explanation for the absorption is that the $10 \mu\text{m}$ dust continuum produced by the emission region within the disk, is absorbed by small grains that are present in the surface layers. The $10 \mu\text{m}$ emission region migrates upward with increasing power law index. This behavior is explained by the upward displacement of the surface of the optically thick dust layers from which the $10 \mu\text{m}$ emission emanates. Its radial extension strongly increases with larger power law indices. This is explained through the decrease in the dust temperature gradient at the surface of the optically thick dust layers. The results in larger extension that contains the conditions for the $10 \mu\text{m}$ emission. Additionally, large decreases in the average grain size gradient enhance the amount of small grains in the emission region. Hence, the increase in peak strength of the silicate feature with increasing power law indices can be ascribed to the combined effect of an increase in the amount of small dust grains, as well as to the enhanced radial extension of the emitting region.

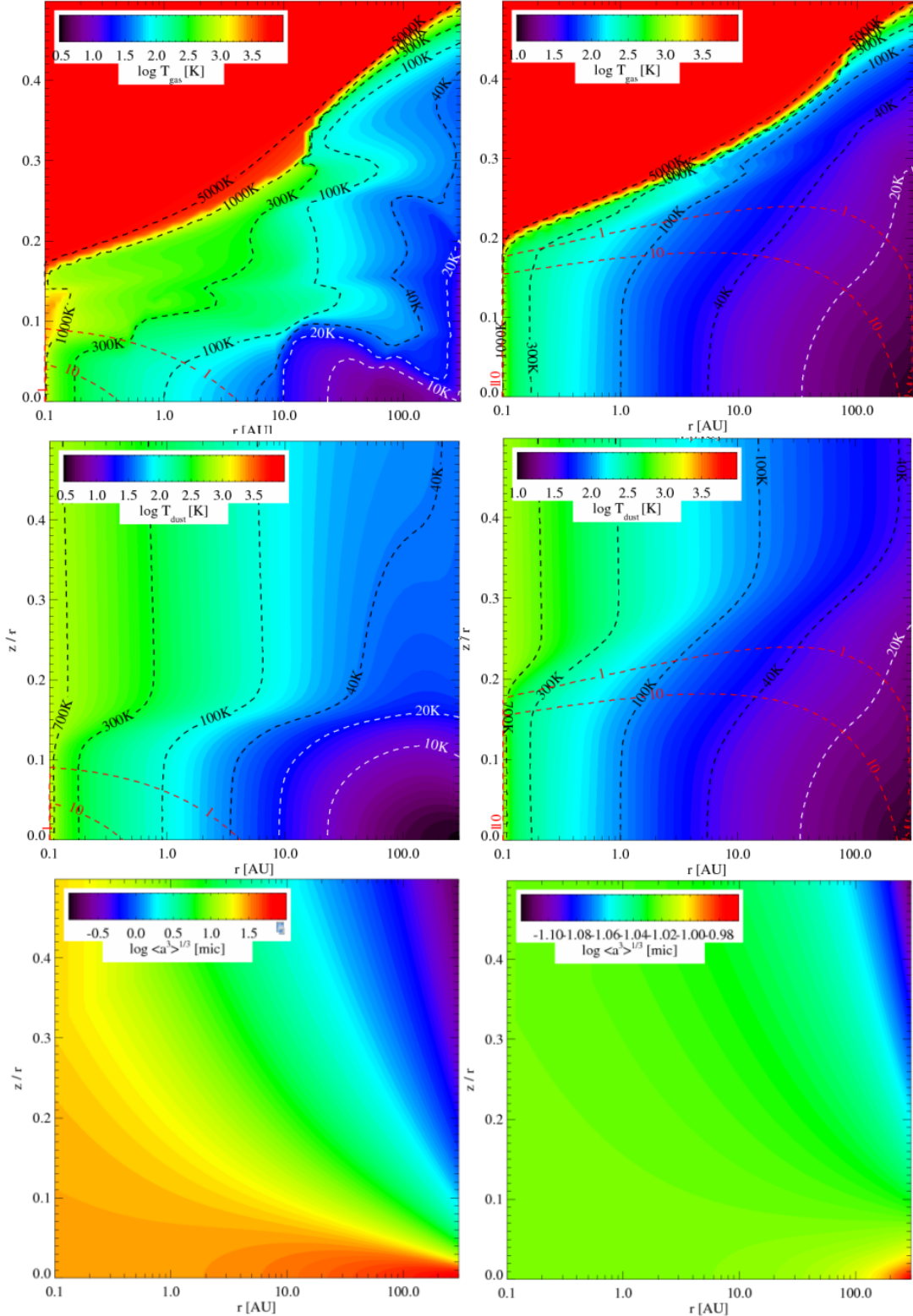


Figure 16: Left column represents $a_{pow} = 2.0$; the right column represents $a_{pow} = 4.5$. Top: Distribution of gas temperatures; middle: Distribution of dust temperatures; bottom: Average grain size distribution. Red dashed lines represent the visual extinction $A_V = 1$ and 10 respectively. Note that color scales vary between the figures.

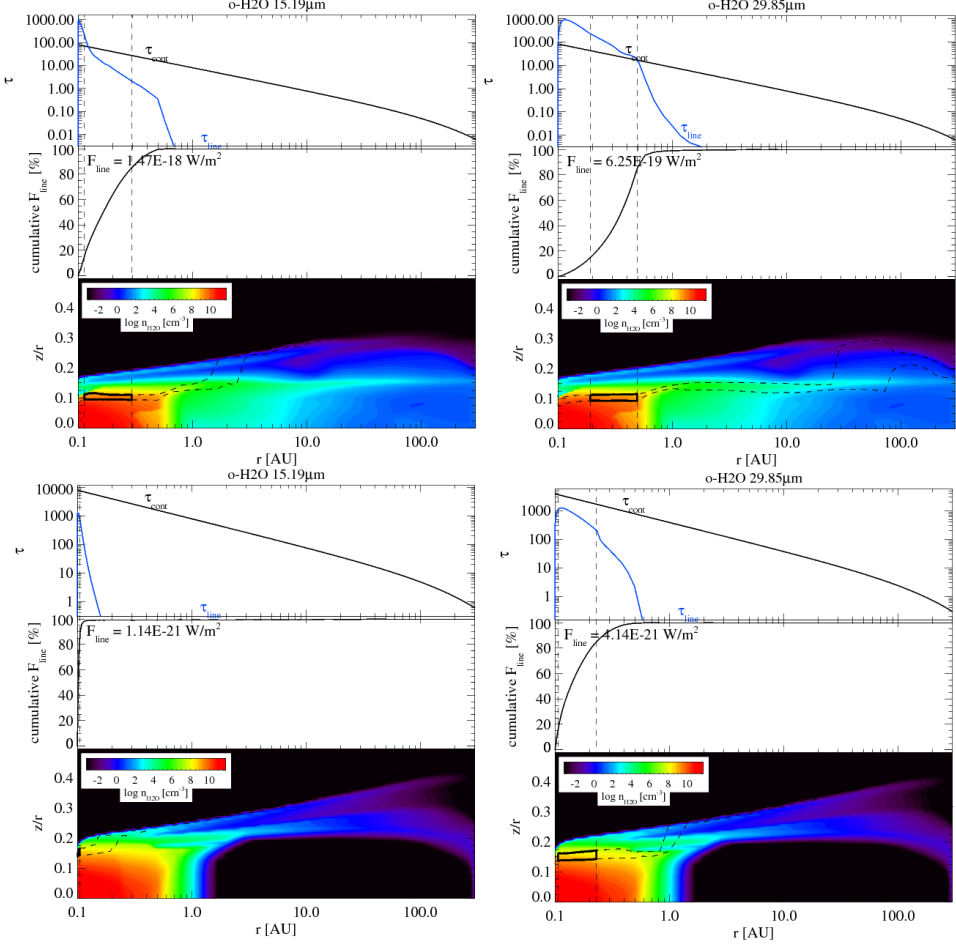


Figure 17: Analysis of the lines $\text{o-H}_2\text{O } 15.19 \mu\text{m}$ left column and $\text{o-H}_2\text{O } 29.85 \mu\text{m}$ right column. The top row shows the results for the 2.0 power-law index and the bottom row shows the results for the 4.5 power-law index. Each figure shows an opacity plot that contains information about the continuum and line optical depth on top, the cumulative line flux (middle), and a plot containing the distribution of water and the region (black box) where 15–85% of line emission originates from (bottom). The grey dashed lines indicate the radial and vertical extent of the emitting region in all the plots.

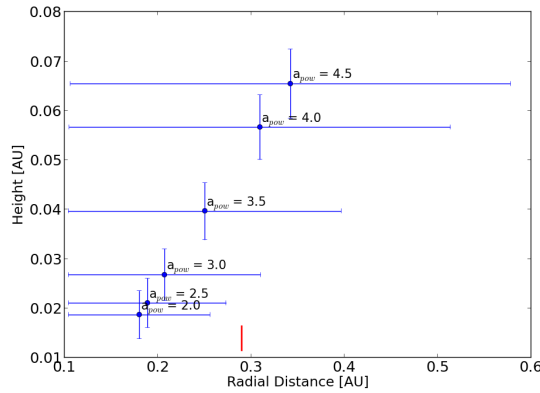


Figure 18: The extent and position of the $10\mu\text{m}$ emission region from which 15–85% of the $10\mu\text{m}$ emission arises for the power law indices in this series. The red bar indicates the radial location of the $10\mu\text{m}$ emission region according to Kessler-Silacci et al. (2007), this only indicates the radial positions and contains no information about the vertical extent

4.3 Variation of the disks gas mass

Having studied how mid-IR water emission and the peak strength of the $10\ \mu\text{m}$ silicate feature correlate for effects of varying dust properties, effects of changing the disks gas mass will be studied in the following. Young protoplanetary disks contain most of their mass in the form of gas. Thus, gas masses represent an import aspect of protoplanetary disks. As there are large variations in the mass of proptoplanetary disks, it is important to understand how this affects the disk. In this series of varying gas masses, the dust mass is kept constant at $10^{-4}\ M_{\odot}$. The model has been calculated for gas masses (M_{gas}) of $10^{-5}, 10^{-4}, 10^{-3}, 0.01, 0.05$ and $0.1\ M_{\odot}$. Modeled spectra in the Spitzer range for these gas masses are shown in Appendix C. With increasing gas mass, in particular for large masses, the theoretical Spitzer spectra show a large increase in molecular emission line fluxes. The blends with their corresponding Gaussian fits are shown in Fig. 19, the same blends widths as previously mentioned are used. The result is shown in Fig. 20 in which integrated water blend fluxes are plotted together with peak strengths of the $10\ \mu\text{m}$ silicate feature. Resulting values from this model series are listed in Table 8. We note that integrated water blend fluxes strongly increase with increasing gas mass.

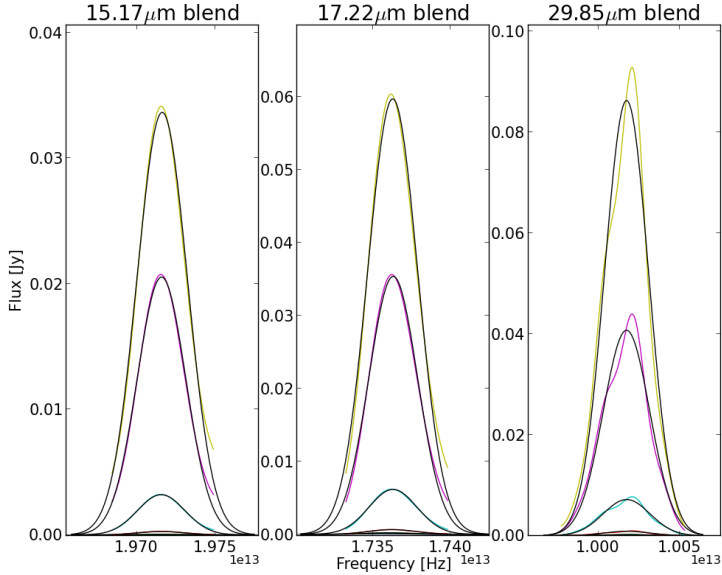


Figure 19: Water line blends with their corresponding Gaussian fitted profiles. Each color represents a blend corresponding to a spectrum of a particular gas mass. The gas mass decreases from top to bottom. The corresponding Gaussian fitted profiles are shown in black.

Table 8: Results for different gas masses

M_{gas} [M_{\odot}]	$15.17\ \mu\text{m}$ blend flux [$\text{erg cm}^{-2}\ \text{s}^{-1}$]	$17.22\ \mu\text{m}$ blend flux [$\text{erg cm}^{-2}\ \text{s}^{-1}$]	$29.85\ \mu\text{m}$ blend flux [$\text{erg cm}^{-2}\ \text{s}^{-1}$]	peak strength of the $10\ \mu\text{m}$ silicate feature
10^{-5}	$2.20 \cdot 10^{-18}$	$4.00 \cdot 10^{-17}$	$4.05 \cdot 10^{-17}$	0.35
10^{-4}	$1.77 \cdot 10^{-17}$	$8.55 \cdot 10^{-17}$	$7.78 \cdot 10^{-17}$	0.24
10^{-3}	$1.04 \cdot 10^{-16}$	$2.55 \cdot 10^{-16}$	$3.04 \cdot 10^{-16}$	0.20
0.01	$1.22 \cdot 10^{-15}$	$2.39 \cdot 10^{-15}$	$2.57 \cdot 10^{-15}$	0.18
0.05	$8.00 \cdot 10^{-15}$	$1.40 \cdot 10^{-14}$	$1.45 \cdot 10^{-14}$	0.18
0.1	$1.36 \cdot 10^{-14}$	$2.42 \cdot 10^{-14}$	$2.91 \cdot 10^{-14}$	0.19

Peak strengths of the $10\ \mu\text{m}$ silicate feature are initially decreasing with increasing gas mass. However at large gas masses, peak strengths of the silicate feature cease to change. To get an understanding of this trend, various properties of the disk structure will be studied. Continuum dust opacities do

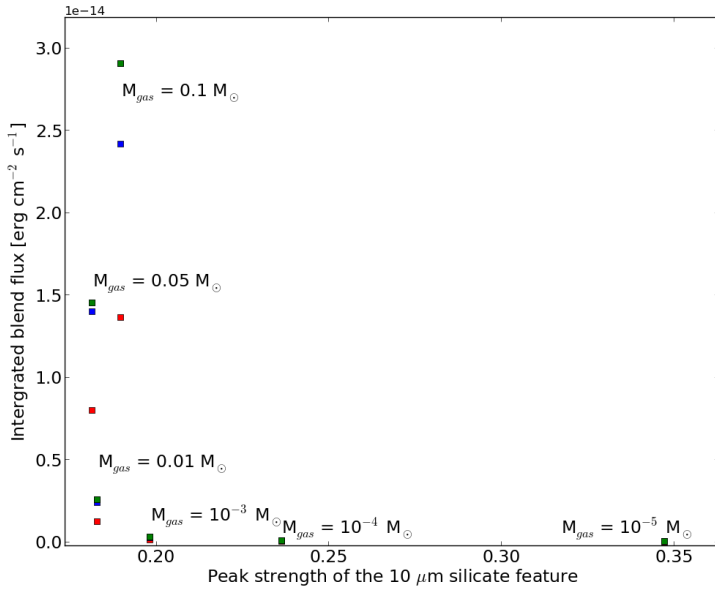


Figure 20: Water blend fluxes versus the peak strength of the $10\text{ }\mu\text{m}$ silicate feature for all gas masses. Red indicates the $15.17\text{ }\mu\text{m}$ blend, blue the $17.22\text{ }\mu\text{m}$ blend and green the $29.85\text{ }\mu\text{m}$ blend.

not show any noticeable change, which is a consequence of the fact that the dust mass is constant and that the properties of dust are not altered. Gas temperature distributions for gas masses of 10^{-5} and $0.1\text{ }M_{\odot}$ within the disk are shown in Fig. 21. It shows that various properties of the disk such as the gas temperature distribution depend on the gas mass. With increasing gas mass, densities within the disk strongly increase. These large changes in density are visible in Fig. 21, which shows the average particle density structure within the disk. Densities significantly increase in the vertical as well as in the radial direction. This results in lower gas temperatures at larger heights within the disk. As the warm gas layers become vertically more extended, upper regions of these warm gas layers become increasingly transparent, this is seen in Fig. 21 in which the height of this region above the $A_V = 1$ extinction line increases. Therefore, gas temperatures within these warm layers are enhanced radially as well as vertically resulting in a lower gas temperature gradient in these regions. We notice that the gas mass strongly affects the line emitting regions. An overview of properties of the line emitting regions is listed in Table. 9, and shown in Fig. 22. Analysis of the line emitting regions for a gas mass of $10^{-5}M_{\odot}$ is omitted because of the fact that the o-H₂O $15.19\text{ }\mu\text{m}$ emission region was not properly resolved in this extreme model. Densities in the emitting regions significantly increase as a consequence of increased gas masses. Increasing the gas mass from 10^{-4} to $0.1\text{ }M_{\odot}$ results in an increase in average o-H₂O density by two orders of magnitude for the o-H₂O $15.19\text{ }\mu\text{m}$ and one order of magnitude for the o-H₂O $29.85\text{ }\mu\text{m}$ line emission region. Subsequently, the geometry and position of the line emitting regions is strongly affected. The $15.19\text{ }\mu\text{m}$ and $29.85\text{ }\mu\text{m}$ emission regions show similar changes. Both emission regions migrate to larger heights with increasing gas masses, which is explained by the increased vertical extension of the regions that contain warm gas. Increases in the radial extension of the emitting regions is induced by decreases in gas temperature gradients. The o-H₂O $15.19\text{ }\mu\text{m}$ emission region increases by a factor of 20 in area and the o-H₂O $29.85\text{ }\mu\text{m}$ emission region by a factor of 30 in changing the gas mass from 10^{-4} to $0.1\text{ }M_{\odot}$. Large increases in water vapor volume densities result in large line optical depths within the emitting regions. A consequence of this is that line fluxes from these regions decline. The fact that we see strong increases in water blend fluxes although line optical depth increases, is explained by the fact that large enhancements in area dominate over the diminishing effect of large line optical depths. The explanation for the fact that peak strength of the $10\text{ }\mu\text{m}$ silicate feature changes although the dust mass is kept constant, is the interaction of dust and gas. For low gas masses, the peak strength of the $10\text{ }\mu\text{m}$ silicate feature increases, which is explained by dust settling. With decreasing gas masses, settling of dust increases because there is a lower degree of drag force from the gas counteracting the

Table 9: Properties of the water line emission regions

Line at $M = 0.0001 M_{\odot}$	$\text{o-H}_2\text{O } 15.18890 \mu\text{m}$	$\text{o-H}_2\text{O } 29.85089 \mu\text{m}$
Average $\text{o-H}_2\text{O}$ density [cm^{-3}]	$6.23 \cdot 10^8$	$3.65 \cdot 10^8$
Radial extension [AU]	$0.102 - 0.107$	$0.105 - 0.170$
Vertical extension [AU]	$0.014 - 0.012$	$0.017 - 0.015$
Gas Temperature [K]	878.49	445.66
Dust Temperature [K]	875.45	445.93
Line at $M = 0.1 M_{\odot}$		
Average $\text{o-H}_2\text{O}$ density [cm^{-3}]	$3.17 \cdot 10^{11}$	$6.87 \cdot 10^9$
Radial extension [AU]	$0.102 - 0.177$	$0.197 - 0.758$
Vertical extension [AU]	$0.021 - 0.020$	$0.066 - 0.060$
Gas Temperature [K]	397.68	203.22
Dust Temperature [K]	397.56	202.59

settling of dust grains. This will cause large dust grains to settle towards the mid-plane since they are weakly coupled to the gas. Small grains barely settle, with the consequence that only small grains will reside in the upper layers of the disk. The effect of dust settling on the distribution of average grain sizes within the disk is shown in Fig. 21. In this distribution for the lowest gas mass, the large degree of dust settling becomes visible through a large gradient in average grain size from the mid-plane to the upper layers. The result is that all large grains are settled on the mid plane and only small grains are present in upper layers. This explains why dust temperatures are higher in the upper layers in the inner regions for low gas masses. On the contrary, we can see that the distribution of grain sizes for large gas masses is much more homogeneous. The influence of this on the $10 \mu\text{m}$ emission region becomes visible in Fig. 23. Here, the $10 \mu\text{m}$ emission region for the range of gas masses is shown. The location of the $10 \mu\text{m}$ emission region is overall in agreement with the relation for the silicate emission zone that was found by Kessler-Silacci et al. (2007), this radial location is shown in Fig. 23. This emission region migrates upwards with increasing gas mass. This is the result of small grains that can remain in the upper layers because these are strongly coupled to gas. A decrease in the amount of dust settling causes the average grain sizes in the emitting region to be larger for larger gas masses. This will reduce the $10 \mu\text{m}$ flux that originates from this region. The increased radial extension of the $10 \mu\text{m}$ emission region is caused by a decrease in the dust temperature gradient. We conclude that even though the $10 \mu\text{m}$ emission region increases slightly in radial extension, the effect of larger grains in this region will dominate and hence decrease the flux. The fact that the peak strength of the $10 \mu\text{m}$ silicate feature ceases to increase for the largest gas masses, is explained by the fact that the distribution of average dust grains sizes is not noticeably changing anymore. It is noticed that for the largest gas mass the peak strength of the silicate feature increases. This is an increase of 4.5% in the peak strength of the $10 \mu\text{m}$ silicate feature corresponding to a change in gas mass from $0.05 M_{\odot}$ to $0.1 M_{\odot}$. This is small compared to changes in the order of 100 % for the power law index series, but rather large compared to changes in the order of 1 % for the series of maximum dust grain size. Therefore it remains uncertain whether this change can be ascribed to numerical uncertainties in this model or that there is an unexpected behavior in the trend.

4.4 Variation of the central star

In the previous series the central star was unaltered. Since many protoplanetary disks host different central stars, we are interested how the dust emission of the disk will be affected through variation of the central star. Therefore, the effect of different central stars on the peak strength of the $10 \mu\text{m}$ silicate feature will be studied. We will explore the effect of central stars having spectral classes of A8V, F5V, F8V, G0V, K5V, M2V and M6. The values for the physical properties of these stars are derived from real stars (Antonellini et al., 2015a, under revision). Throughout this series, properties of dust and gas are left unaltered. As these stars have different bolometric and FUV luminosities, the dust in this disk will be exposed to radiation fields of varying intensities. The $10 \mu\text{m}$ silicate feature peak strength is determined as previously described. We note however that the A8V, F5V and F8V stars have luminosities that are unusually high for T Tauri stars, and more appropriate for Herbig Ae stars.

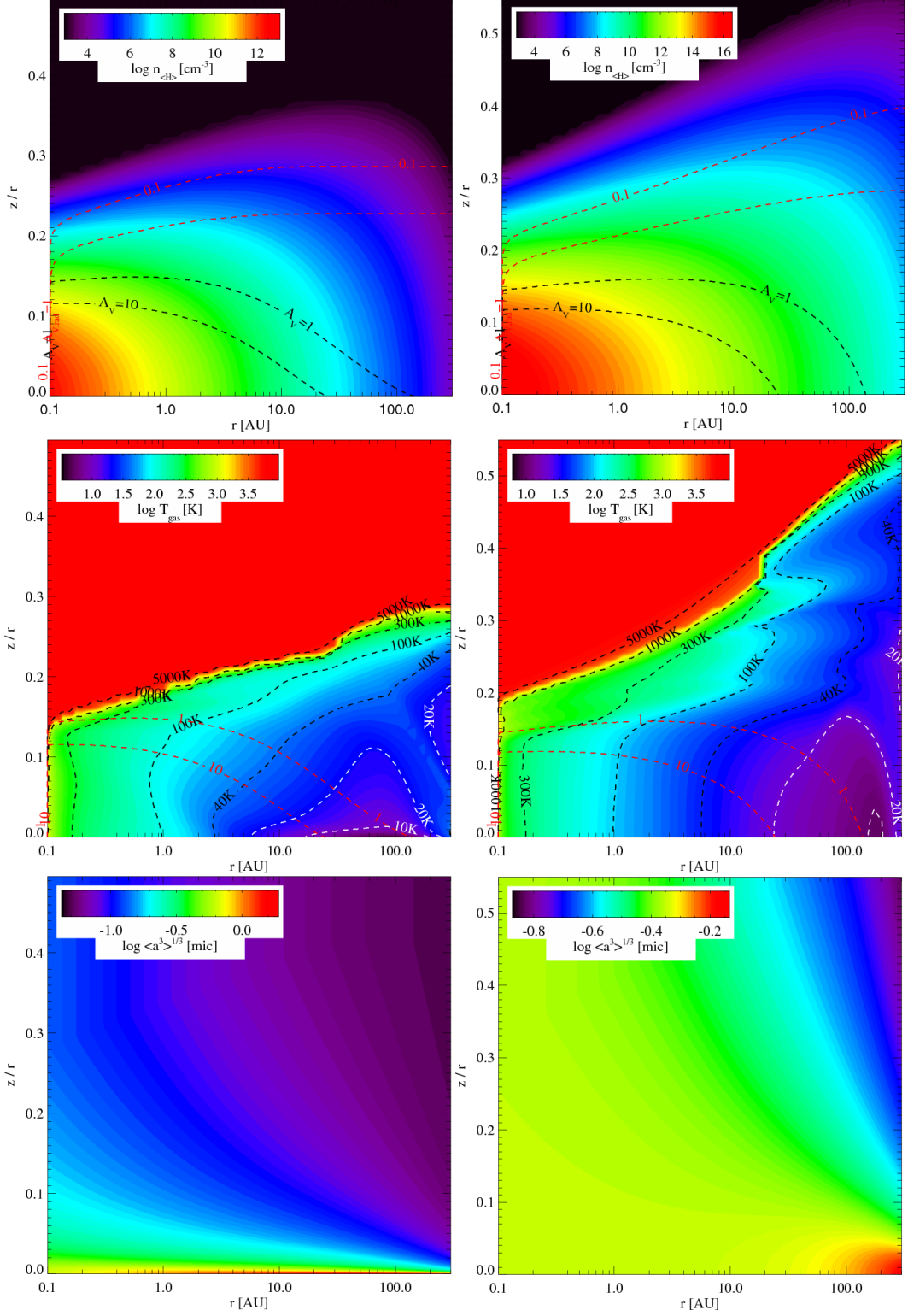


Figure 21: Left column represents $M_{gas} = 10^{-5} M_{\odot}$; the right column represents $M_{gas} = 0.1 M_{\odot}$. Top: The average particle density structure in which the black dashed lines represent the visual extinction A_V of 1 and 10 and the red dashed lines show the radial visual extinction $A_{V,rad}$ of 0.1 and 1 respectively.; middle: Distribution of gas temperatures; bottom: Average grain size distribution. Note that color scales vary between the figures.

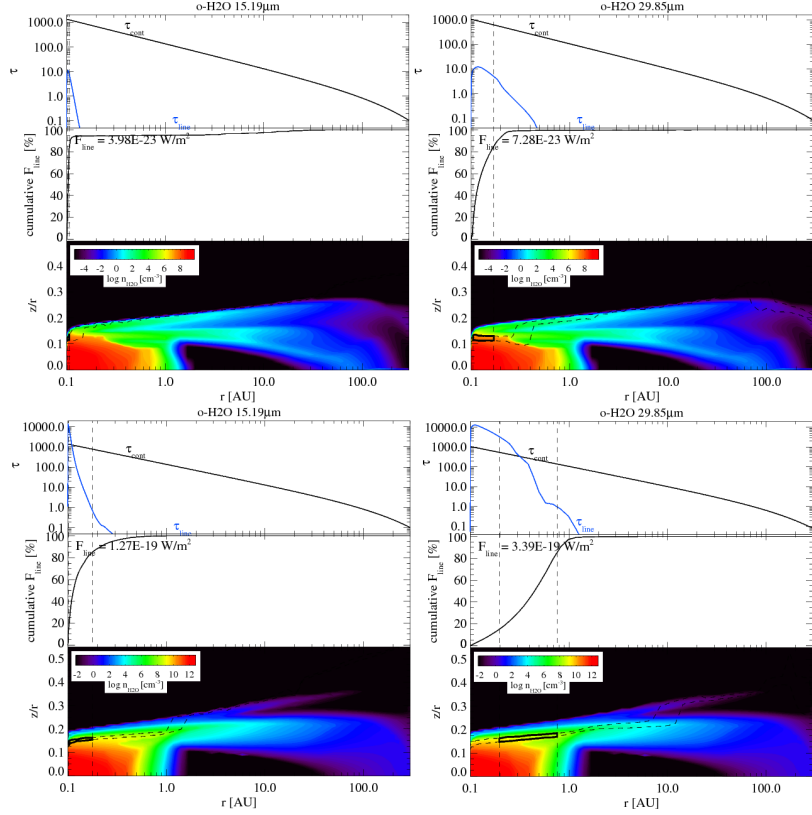


Figure 22: Analysis of the lines $\text{o-H}_2\text{O } 15.19 \mu\text{m}$ left column and $\text{o-H}_2\text{O } 29.85 \mu\text{m}$ right column. The top row shows the results for a gas mass of $10^{-4} M_{\odot}$ and the bottom row shows the results for a gas mass of $0.1 M_{\odot}$. Each figure is represented by an opacity plot that contains information about the continuum and line optical depth (top), the cumulative line flux (middle) and a plot containing the distribution of water and the region (black box) where 15-85% of line emission originates from (bottom). The grey dashed lines indicate the radial and vertical extent of the emitting region in all the plots

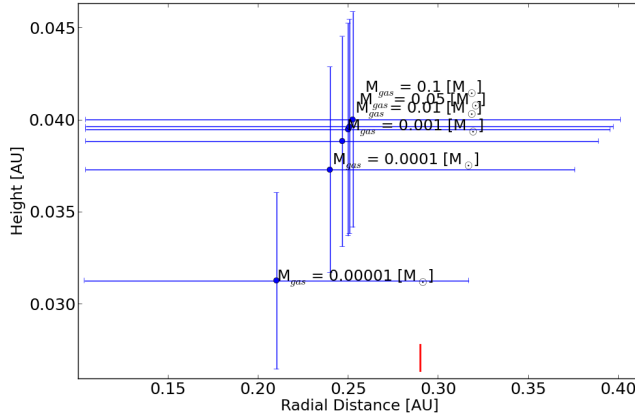


Figure 23: The extent and position of the $10 \mu\text{m}$ emission region from which 15-85% of the $10 \mu\text{m}$ emission arises. The red bar indicates the radial location of the $10 \mu\text{m}$ emission region according to Kessler-Silacci et al. (2007), this only indicates the radial positions and contains no information about the vertical extent.

The result is shown in Fig. 24, in which the peak strength of the $10\ \mu\text{m}$ silicate feature versus the bolometric luminosity is plotted. We find peak strengths of the $10\ \mu\text{m}$ silicate feature of 0.03 for the M2V star, up to 0.30 for the F8V star. There is a clear correlation between the peak strength of the $10\ \mu\text{m}$ silicate feature and the bolometric luminosity. No correlation is found between the peak strength of the $10\ \mu\text{m}$ silicate feature and the FUV luminosity.

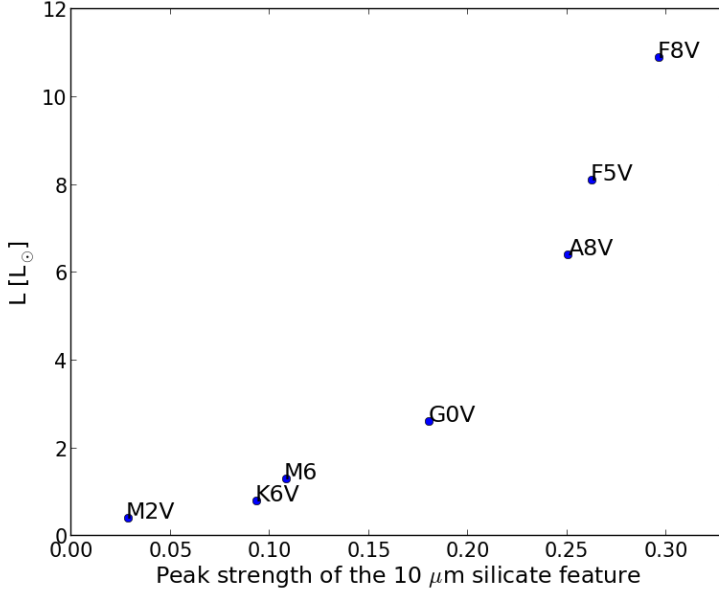


Figure 24: Peak strength of the $10\ \mu\text{m}$ silicate feature versus the bolometric luminosity for a range of central stars.

4.5 Comparing modeled series

An enhanced insight in protoplanetary disks, requires the understanding of the role of investigated parameters in the structure and emission of protoplanetary disks. Therefore we compare the different model series in order to investigate the extent to which the mid-IR water blends fluxes and the peak strength of the $10\ \mu\text{m}$ silicate feature are influenced by these parameters.

Table 10: Ranges of the results from observations and model series

	water blend flux range [$\text{erg cm}^{-2}\ \text{s}^{-1}$]	peak strength range of the $10\ \mu\text{m}$ silicate feature
Observations	$0.20 \cdot 10^{-14}$ - $8.05 \cdot 10^{-14}$	0.13-2.90
a_{\max} series	$5.58 \cdot 10^{-16}$ - $1.97 \cdot 10^{-14}$	0.176-0.190
a_{pow} series	$2.55 \cdot 10^{-16}$ - $6.43 \cdot 10^{-14}$	0.05-0.53
M_{gas} series	$2.20 \cdot 10^{-18}$ - $2.91 \cdot 10^{-14}$	0.18-0.35
Central star series	...	0.03-0.30

Ranges of the results of the modeled series are shown in Table. 10. By comparing these results for the peak strength of the silicate feature, we conclude that of the two dust parameters the power law index affects the peak strength of the silicate feature most strongly. This tells us that the amount of small grains has a larger dependence on the power law index compared to the maximum grain size. Out of all modeled series, the power law index series shows the largest variation in the peak strength of the silicate feature. The maximum grain size parameter has the least effect on the peak strength, and varies over a range that is an order of magnitude smaller compared to the other series. This small range is

explained by the fact that the power law index is kept constant at a value of 3.5. As the dust mass is dominated by large grains, the amount of small grains decreases because of the fact that the dust mass is held constant. However, the constant power law index results in the fact that the amount of large grains strongly decreases as they become larger. Therefore, the small relative differences in maximum grain sizes for the major part in this series, results in the fact that the amount of small grains is not altered to a great extent translating in to small differences in the peak strength of the silicate feature. As opposed to the other model series, the change of the peak strength in the gas mass series in which the properties of the dust are kept constant is caused solely by variations in the distribution of dust grains throughout the disk. The fact that the peak strength of the silicate feature is not only changing with variations in dust properties but in addition is altered through variations of gas mass and central star, tells us that the peak strength of the $10\text{ }\mu\text{m}$ silicate feature is not solely determined by the properties of dust itself.

Various ranges of water blend fluxes are encountered in the model series (Table. 10). The main driver behind the changes in water blend fluxes in these series is the changing gas temperature structure which sets the extension of the emission regions. Gas temperature structures are affected in the same way for the various model series. This translates into the fact that all model series in which water lines were studied, show increased differences between the 15.17 , 17.22 and $29.85\text{ }\mu\text{m}$ blend fluxes with decreasing peak strength of the $10\text{ }\mu\text{m}$ silicate feature. Largest variations in water blend fluxes are found for the gas mass series, which is two orders of magnitudes larger compared to the series of dust parameters. This shows that besides the properties of dust, the gas mass plays a role in the extent of mid-IR water emission. The least variation in water blend fluxes is found for the maximum dust grain series. For the dust and gas model series we find that the mid-IR water emission and the peak strength of the silicate feature correlate in the same fashion in which the peak strength of the silicate feature increases as the integrated water blend fluxes decrease. The power law index shows the strongest correlation between the mid-IR water blend fluxes and the peak strength of the silicate feature. The model series show that the mid-IR water emission originates from the same disk regions as the $10\text{ }\mu\text{m}$ silicate feature.

5 Comparison of observations with the models

To get a better understanding of protoplanetary disks, it is important to know to what extent the model describes the reality. Therefore it is important to compare the results of the model with the results from real observations. The model provides us with a clear anti correlation between the integrated mid-IR water blend fluxes and the peak strength of the $10\text{ }\mu\text{m}$ silicate feature. Observations on the contrary show no signs of a correlation but rather a scatter in which these sources show different behavior. The main explanation for this difference lies in the fact that we compare the observed protoplanetary disks which consist of a large variety of disks to a single model. In reality, various parameters change simultaneously and are coupled to each other, whereas in the model series only one parameter is varied leaving the others unchanged.

The range of mid-IR water blend fluxes that is found from the observational data is shown in Table. 10. The majority of the sources however is found below $2.0\text{ erg s}^{-1}\text{ cm}^{-2}$. Ranges in water blend fluxes of the modeled series are listed in Table. 10. When comparing these values to the observed ones, we find that for low opacities e.g. large maximum grain sizes and low power law indices that the values are in good agreement with observations. However, for large dust opacities we find integrated water blend fluxes that are an order of magnitude smaller. Considering the variation of gas masses, we find that for large gas masses the values are in good agreement with the observations, for low gas masses however we find integrated blend fluxes that are orders of magnitudes smaller. This large difference with the observed values is explained by the fact that for the lowest gas masses, the dust mass is even larger or equal to the gas mass. This is not realistic since masses of protoplanetary disks are dominated by gas. In the models we find that the integrated water blend fluxes for $15.17\text{ }\mu\text{m}$ are significantly smaller than the 17.22 and $29.85\text{ }\mu\text{m}$ blend fluxes. In addition, results of the model show that the $29.85\text{ }\mu\text{m}$ blend has the largest fluxes. Comparing this to the observations, we find this is only consistent for a few sources, the majority of observed sources show the strongest water blend fluxes for the $17.22\text{ }\mu\text{m}$ blend. A possible contribution to the differences that we observe in the properties of mid-IR water emission is the fact that the model does not take into account complex processes such as turbulent mixing and

accretion which could lead to differences in emission. As the water blend widths used by Pontoppidan et al. (2010) are not indicated, one has to take into account the possibility that Pontoppidan et al. (2010) chose different widths for the blends compared to the ones adopted in this study, resulting in a different amount of lines within the blends. This could lead to differences in blend fluxes between the ones reported from observations and derived here from the model. For an improved comparison in the future, the same blend width should be used.

Ranges from the models and observations for the peak strength of the silicate feature are listed in Table 10. Comparing these values, we find two cases in which the values are in good agreement with the observations. These are, the series of varying power law indices for the power law index 4.0 and 4.5 and the lowest gas mass in the series of varying gas masses. For lower power law indices, higher gas masses and for the series of varying the maximum grain size we find that these values are comparable to the lowest value that is observed and are about a factor of 2-3 smaller than the majority of the observed values. For the series of varying central star, we find that for the stars with luminosities compared to the observed sources the peak strength of the silicate feature is up to a magnitude smaller than the observed values. The range of peak strengths in the model series for the variation of maximum grain size is orders of magnitudes smaller than the variation of the peak strength of the silicate feature in the observed sample. This is most likely explained by the fact that this series only traces small steps in the evolution of dust, whereas in reality it is most likely that disk with larger differences in dust evolution are found. In addition, the model does not take crystallinity into account.

From the model series of different central stars, a correlation between the bolometric luminosity and the peak strength of the silicate feature was found. This correlation resembled an increase in the peak strength of the silicate feature with increasing luminosity. A contribution to the absence of this correlation in the observed sources, is most likely the fact that the observed sample of disks are in different stages of their dust evolution. As opposed to the disk model studied here, where the properties of the dust are unaltered. As for the observations, no correlation is found between the FUV luminosity and the peak strength of the silicate feature in the model series of different central stars.

Significant variations in the silicate feature are observed by observations at different epochs for some actively accreting TTauri stars (Bary et al., 2009). One has to account to the possibility that some sources could have been observed during a highly active phase, resulting in values that are not representative compared to the sources which are in a passive state. To get a result that is statistically more reliable, larger samples of sources are needed. Besides, a larger sample of sources would enhance the insight in a possible correlation. Detailed analysis of these individual objects is needed to provide an improved insight in whether and how the mid-IR water emission relates to the peak strength of the silicate feature.

6 Conclusion

The aim of this thesis was to investigate whether there is a correlation between the mid-IR water emission and the peak strength of the $10\text{ }\mu\text{m}$ silicate feature. This has never been investigated before in the literature. Part of this work consisted of the analysis of observational data from various TTauri disk systems. Besides, the effects of various properties on the disk structure and the $10\text{ }\mu\text{m}$ silicate feature were investigated using ProDiMo.

Observed sources in which water was detected (Pontoppidan et al., 2010) were selected for this study. Mid-IR water blend fluxes for the blends 15.17 , 17.22 and $29.85\text{ }\mu\text{m}$ were used from the work of Pontoppidan et al. (2010). Spitzer spectra were acquired for the selected sources in order to analyze the $10\text{ }\mu\text{m}$ silicate feature. Analysis of the $10\text{ }\mu\text{m}$ silicate feature was achieved through subtraction of the local continuum that was represented by a linear fit. As the peak strength is sensitive to the properties of dust, it was used throughout this thesis and was determined through division of the peak flux of the silicate feature by the local continuum. No correlation was found between the mid-IR water emission and the peak strength of the $10\text{ }\mu\text{m}$ silicate feature for the collection of TTauri disk systems. However, we found disks (case 2) with large variations in peak strength of the silicate feature in a small range of water blend fluxes, whereas other disks (case 1) showed large variations in water blend fluxes in a small range of peak strengths of the silicate feature. We explain case 1 behavior by the effect of different luminosities, and FUV fields (as a consequence of different accretion rates) on the mid-IR water emission. We showed that the majority of sources with lower peak strengths of the $10\text{ }\mu\text{m}$ silicate feature contain crystallized dust.

Effects of various parameters on the mid-IR water emission of the blends 15.17 , 17.22 and $29.85\text{ }\mu\text{m}$ and the peak strength of the $10\text{ }\mu\text{m}$ silicate feature were simulated using the ProDiMo model. Evolution of grain growth was simulated through variations in maximum grain size and power law index of the dust size distribution. Maximum dust grain radii were varied from 250 up to $10^5\text{ }\mu\text{m}$. Power law indices in the range of 2.0 - 4.5 were simulated. In addition to the variations in the properties of dust, effects of changing the disks gas mass in the 10^{-5} - $0.1\text{ }M_\odot$ range were explored. Leaving disk properties unaltered, the influence of different central stars of type M2V to F8V on the peak strength of the $10\text{ }\mu\text{m}$ silicate feature was investigated. We showed that out of these modeled parameters, the peak strength of the $10\text{ }\mu\text{m}$ silicate feature is most affected by the power law index. Variations in maximum grain size showed the least amount of variation in the peak strength of the $10\text{ }\mu\text{m}$ silicate feature. Through variations in the central star, the peak strength of the $10\text{ }\mu\text{m}$ silicate feature was shown to be proportional to the bolometric luminosity. In the model series, variations of these parameters resulted in changes in transparency of the disk as a result of different dust opacities in the dust model series and changes of the extension of the region containing warm gas in the gas mass series. Therefore, we found that these parameters significantly alter the gas temperature distribution within the disk. These variations resulted in changes of the gas temperature gradient which sets the extent of the regions that host the conditions for the mid-IR water emission lines in question. This led to variations in the amount of mid-IR water emission with the major contribution being the differences in radial extensions of the emitting regions. The largest variation in the mid-IR water emission was found for the variation of the gas mass, whereas variation in maximum dust grain radii showed the least amount of variation. For the model series in which the mid-IR emission of water was studied, we found an anti-correlation between the peak strength of the $10\text{ }\mu\text{m}$ silicate feature and the mid-IR water emission. The strongest anti-correlation was found for variations in the power law index of the dust size distribution.

The results show that the majority of the values that were modeled using ProDiMo, e.g. mid-IR water emission and the peak strength of the $10\mu\text{m}$ silicate feature are in good agreement with the observed values. We note however that models easily provide trends because of the fact that only one parameter is changed at a time. This is not the case in reality, because the disk we observe vary in many properties. Clear correlations that are found from one specific model are most likely distorted in reality. Another fact that complicates this study is that the $10\text{ }\mu\text{m}$ silicate feature traces dust in a very small and thin surface layer. This could account for distortions of the view on the properties of dust in the disk regions of interest. Homogeneity of dust throughout the disk is assumed in our models which could be different from reality. Determining a correlation from observations remains difficult because of large variations between disks that are observed.

Although we found that the mid-IR water emission increases with increasing gas mass, our findings show that the amount of mid-IR water emission strongly depends on the properties and distribution of dust within the disk. Therefore, the amount of mid-IR water emission is not per se reflecting the abundance of water present in these regions of protoplanetary disks.

The real nature of protoplanetary disks seems to be more complex than the model suggest. Future research on the nature of these individual disks with the James Web Space Telescope etc. is needed to get an enhanced understanding on the link between the mid-IR dust emission and water emission. A collection of 100 TTauri disk systems would give a better insight in the connection between the mid-IR water emission and the silicate feature. For future studies, it would be good to select sources with similar values in the properties that contribute to differences in the mid-IR water and dust emission. This selection would consist of sources with central stars that show little variation in luminosity and accretion rates. In addition it would be good to find sources with similar degrees of flaring index to decrease to degree to which the geometry of disks influences the results. For this selection, a good representation would require sources that are evenly sampled over large range of peak strengths of the silicate feature.

7 Acknowledgments

I would like to thank my supervisor Inga Kamp for this interesting research project, in particular for all her time and support throughout this research project. For the explanation of concepts and help with problems that were encountered, and the support in writing this thesis. In addition I want to thank Stefano Antonellini for his support with answering questions and supporting with the model. Further, I want to thank Fred Lahuis for providing spectra and suggestions.

8 Literature

References

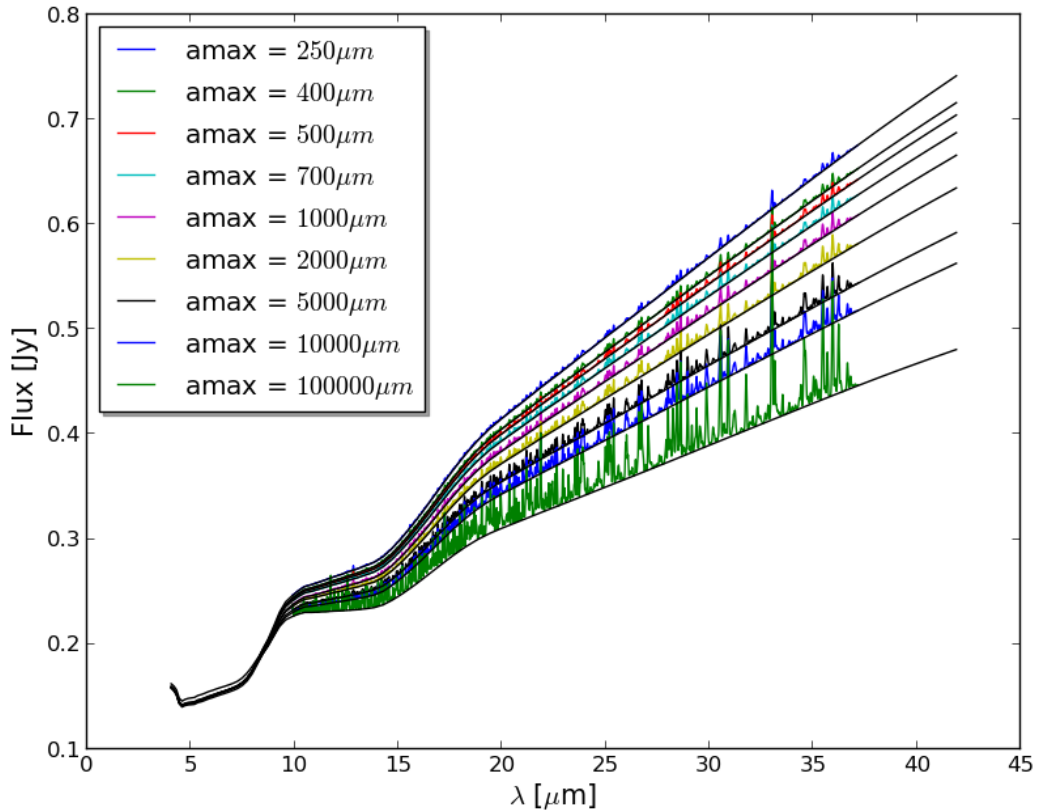
- Adams et al. (1987). Spectral evolution of young stellar objects. *The Astrophysical Journal*, 312:788–806.
- Antonellini et al. (2015a). Mid-ir spectra of pre-main sequence stars: an explanation for the non-detections of water lines. *Astronomy and Astrophysics*.
- Antonellini et al. (2015b). Understanding the water emission in the mid- and far-ir from protoplanetary disks around t tauri stars. *Astronomy and Astrophysics*.
- Bary et al. (2009). Variations of the 10 m silicate features in the actively accreting t tauri stars dg tau and xz tau. *The Astrophysical Journal Letters*, 706:L168–L172.
- Bouwman et al. (2008). The formation and evolution of planetary systems: Grain growth and chemical processing of dust in t tauri systems. *The Astrophysical Journal*, 683:479–498.
- Dionatos (2015). Gas line observations of disks.
- Dullemond et al. (2007). Models of the structure and evolution of protoplanetary disks. *Protostars and Planets V*, University of Arizona Press, pages p.555–572.
- Dullemond and Monnier (2010). The inner regions of protoplanetary disks. *Annual Review of Astronomy and Astrophysics*, 48:205–239.
- Evans et al. (2003). From molecular cores to planet-forming disks: An sirtf legacy program. *The Astronomical Society of the Pacific*, 115:965–980.
- Henning and Semenov (2013). Chemistry in protoplanetary disks. *Chemical Reviews*, 113:9016–9042.
- Kamp and Dullemond (2004). The gas temperature in the surface layers of protoplanetary disks. *The Astrophysical Journal*, 615:991–999.
- Kenyon and Hartmann (1987). Spectral energy distributions of t tauri stars - disk flaring and limits on accretion. *The Astrophysical Journal*, 323:714–733.
- Kessler-Silacci et al. (2005). 8-13 um spectroscopy of young stellar objects:evolution of the silicate feature. *The Astrophysical Journal*, 622:404–429.
- Kessler-Silacci et al. (2007). Probing protoplanetary disks with silicate emission:where is the silicate emission zone? *The Astrophysical Journal*, 659:680–684.
- Lada (1987). Star formation - from ob associations to protostars. *Dordrecht, D. Reidel Publishing Co.*, 914:1–17.
- Lahuis (2007). *Molecular fingerprints of star formation throughout the Universe -a space-based infrared study-*. PhD thesis, University of Leiden.
- Lebouteiller et al. (2011). Cassis: The cornell atlas of spitzer/ infrared spectrograph sources. *The Astrophysical Journal Supplement Series*, 196:8(13pp).
- McCaughrean and O'Dell (1996). Direct imaging of circumstellar disks in the orion nebula. *The Astronomical Journal*, 111:1977.
- Meijerink et al. (2009). Radiative transfer models of mid-infrared h_2o lines in the planet-forming region of circumstellar disks. *The Astrophysical Journal*, 704:1471–1481.
- Mulders (2013). *Radiative Transfer Models of Protoplanetary Disks:Theory vs. Observations*. PhD thesis, University of Amsterdam.
- Natta et al. (2007). Dust in protoplanetary disks: Properties and evolution. *Protostars and Planets V*, University of Arizona Press, pages p.767–781.

- Olofsson et al. (2009). C2d spitzer-irs spectra of disks around t tauri stars iv. crystalline silicates. *Astronomy and Astrophysics*, 507:327–345.
- Olofsson et al. (2010). C2d spitzer-irs spectra of disks around t tauri stars. *Astronomy and Astrophysics*, 520:23pp.
- Poelman (2007). *Emission characteristics of water in the Universe*. PhD thesis, University of Groningen.
- Pontoppidan et al. (2010). A spitzer survey of mid-ir molecular emission from protoplanetary disk i detection rates. *The Astrophysical Journal*, 720:887–903.
- Pontoppidan et al. (2014). Volatiles in protoplanetary disks. *University of Arizona Press*, 914:363–385.
- Salyk et al. (2011). A spitzer survey of mid-ir molecular emission from protoplanetary disks ii correlations and local thermal equilibrium models. *The Astrophysical Journal*, 731.
- Tennyson et al. (2001). Experimental energy levels of the water molecule. *Journal of Physical and Chemical Reference Data Reprints*, 30:No.3.
- Tennyson and Polyansky (1998). Water on the sun: the sun yields more secrets to spectroscopy. *Contemporary Physics*, 39:283 – 294.
- van Boekel et al. (2003). Grain growth in the inner regions of herbig ae/be star disks. *Astronomy and Astrophysics*, 400:21–24.
- van Boekel et al. (2005). A 10 μm spectroscopic survey of herbig ae star disks: grain growth and crystallization. *Astronomy and Astrophysics*, 437:189–208.
- van Dishoeck (2014). Water: from clouds to planets. *University of Arizona Press*, 914:835–858.
- Voshchinnikov et al. (2008). Is the silicate emission feature only influenced by grain size? *Astronomy and Astrophysics*, 483:L9–L12.
- Walsh et al. (2013). Molecular line emission from a protoplanetary disk irradiated externally by a nearby massive star. *The Astrophysical Journal Letters*, 766.
- Williams and Cieza (2011). Protoplanetary disks and their evolution. *Annual Review of Astronomy and Astrophysics*, 49:67–117.
- Woitke, Kamp, and Thi (2009). Radiation thermo-chemical models of protoplanetary disks i. hydrostatic disk structure and inner rim. *Astronomy and Astrophysics*, 501:383–406.
- Yang et al. (2012). A far-ultraviolet atlas of low-resolution hubble space telescope spectra of t tauri stars. *The Astrophysical Journal*, 744:121(19pp).

Appendices

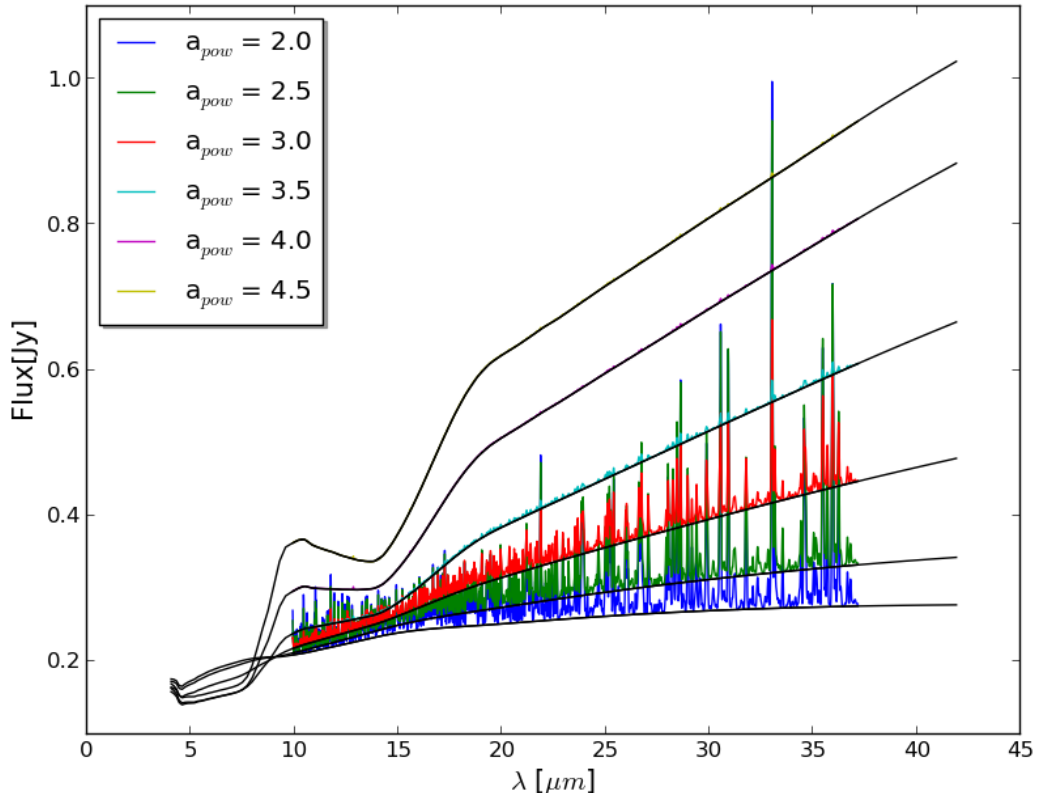
Appendix A

Modeled mid-IR spectra in the Spitzer range for all simulated maximum dust grain radii. Various colors indicate the molecular line blends corresponding to a particular maximum grain radius. The black lines indicate the SED corresponding to each maximum dust grain radius. The SED extends further than the range of the spectrum where it becomes clear that lines are added on top of the SED. The continuum changes as a consequence of different amounts of small dust grains. The $10\ \mu\text{m}$ is clearly visible for all maximum dust grain radii.



Appendix B

Modeled mid-IR spectra in the Spitzer range for all simulated power law indices. Various colors indicate the molecular line blends corresponding to a particular maximum grain radius. The black lines indicate the SED corresponding to each power law index. The SED extends further than the range of the spectrum where it becomes clear that lines are added on top of the SED. The continuum changes as a consequence of different amounts of small dust grains. The $10\ \mu m$ is clearly visible in emission for the power law indices 3.0 to 4.5 and in absorption for power law indices of 2.0 and 2.5.



Appendix C

Modeled mid-IR spectra in the Spitzer range for all simulated gas masses. Various colors indicate the molecular line blends corresponding to a particular gas mass. The black lines indicate the SED corresponding to each gas mass. The SED extends further than the range of the spectrum were it becomes clear that lines are added on top of the SED. The continuum shows substantial changes as a consequence of a different distribution of small dust grains throughout the disk. The $10\ \mu\text{m}$ is clearly visible for all maximum dust grain radii.

